



Validating wind farm parameterizations with offshore SCADA data

Balthazar Arnoldus Maria Sengers¹, Lukas Vollmer¹, and Martin Dörenkämper¹

¹Fraunhofer IWES, Küpkersweg 70, 26129 Oldenburg, Germany

Correspondence: Balthazar Sengers (balthazar.sengers@iwes.fraunhofer.de)

Abstract. A large-scale validation compared wind farm parameterizations (WFPs) of the Weather Research and Forecasting (WRF) model to multi-year SCADA (Supervisory Control and Data Acquisition) data from six offshore wind farms. Although initially seven WFPs were considered, after preliminary assessment only three distinct ones were retained: the original Fitch (Fitch-O), a physics-derived axial induction modification of Fitch (Fitch-pAIM), and the Explicit Wake Parameterization (EWP). The study, conducted at 2 km and 0.67 km resolutions, revealed total energy yield differences of $\pm 5\%$ compared to SCADA data, with finer resolutions having a lower yield due to enhanced internal wake effects. The remainder focused on addressing the main sources of uncertainty affecting the total energy yield. The modeled mean wind speed was likely too low, leading to an energy yield underestimation. Only Fitch-pAIM accurately modeled the power curve and therefore the gross yield, while Fitch-O and EWP underestimated power by neglecting local induction effects. Internal wake magnitudes were well captured by Fitch-O and Fitch-pAIM at fine resolution, while EWP consistently produced too shallow wakes. All WFPs showed signatures of global blockage and a dependency of wake losses on the vertical structure of the boundary layer. Lastly, external wakes were well captured by all parameterizations.

The results demonstrate that Fitch-pAIM outperforms other WFPs at resolutions smaller than the turbine spacing. Despite the limitations in accurately reproducing wake features in narrow wind direction sectors, WFPs accurately capture the total wake loss making their use suitable for AEP calculations.

1 Introduction

One of the key aspects in the planning stage of a new wind farm is assessing the potential power production of a future site. For onshore sites this is typically done by erecting a met mast or deploying a lidar for several months to measure the local wind climate (Rohrig et al., 2019). For offshore sites, such measurement campaigns are considerably more expensive. To supplement the measurements, mesoscale models are often used, either by modeling individual sites of interest directly, or by a previously generated atlases such as the New European Wind Atlas (Hahmann et al., 2020; Dörenkämper et al., 2020).

While the approach of correcting long-term model data sets with short measurement periods has worked well in the last decades, areas like the North Sea will see large changes in the near future with high densities of installed capacity, as offshore wind targets are set to 120 GW by 2030 and 300 GW by 2050 (EU, 2023). With this large number of installed capacity, wind farm or wind farm cluster wake effects will become even more relevant and the influence of future neighboring wind farms on the expected power production of a new or existing farm needs to be accurately represented. As this future wake loss is not



measurable before the farms are built, precise model solutions are essential.

The effect of the offshore wind farm wakes on the power production of downstream wind farms was first shown by Nygaard (2014) and Nygaard and Hansen (2016), demonstrating a drop in generated power of the Nysted wind farm after the upstream Rødsand II wind farm was commissioned. Since then, many studies have observed wind farm wake effects as a reduction of the wind speed or power using observations from met masts (Pettas et al., 2021), satellites (Christiansen and Hasager, 2005; Hasager et al., 2015; Ahsbahs et al., 2020), lidar (Schneemann et al., 2020; Cañadillas et al., 2022), radar (Nygaard and Newcombe, 2018; Ahsbahs et al., 2020), aircraft measurements (Platis et al., 2018; Cañadillas et al., 2020) and turbine data (Mittelmeier et al., 2017; Vollmer et al., 2024b; Sanchez Gomez et al., 2024). The magnitude of the impact of wind farm wakes on other wind farms is dependent on many factors like installed capacity density, distance between farms and meteorological conditions. Lundquist et al. (2019) analyzed the economical impact of wake effects to be several million dollars for an onshore case study in the US, and noted that there is no legal framework to protect existing wind farms. The high relevance of the topic is also evident from legal disputes between operators in the UK (Sanderson, 2025).

Engineering wake models like the Jensen (Jensen, 1983) or Gaussian model (Bastankhah and Porté-Agel, 2014, 2016) are historically the preferred tool for wind resource assessment. However, several studies have reported that such models tend to overestimate the recovery of the wind farm wake (Stieren and Stevens, 2021; Fischereit et al., 2022; Porchetta et al., 2024), although it should be noted that recently advances are being made (Nygaard et al., 2020; Souaiby and Porté-Agel, 2024). Microscale computational fluid dynamics models like Large-Eddy Simulations (LES) have been used for detailed studies on the physics involved (Stieren and Stevens, 2022), and due to computational advances are currently used at coarse resolution for AEP estimates of wind farms (Baas et al., 2023). Due to their comparably low computational effort, the preferred modeling architecture to study wind farm wakes is by using mesoscale Numerical Weather Prediction models, like the established Weather Research and Forecasting model (WRF, Skamarock et al. (2021)). Siedersleben et al. (2018) compared WRF results with aircraft measurements and found a good agreement of the spatial dimensions of the wake, while the magnitude of the simulated wake was sensitive to the background flow. By comparing to scanning lidar data, Cañadillas et al. (2022) demonstrated that the measured wind speed at a met mast inside a wind farm cluster was well represented when wind turbines are modeled in WRF. Studying cluster wakes, Montavon et al. (2024) found that turbine to turbine results are poor, but that on wind farm scale WRF performs well. In a comparison with floating lidar measurements, C2Wind (2025) demonstrated that WRF estimated wind farm wake deficits more accurately than LES and an engineering model. Using WRF, Pryor et al. (2021) estimated wake losses at the Massachusetts cluster to be around 35%. For one farm in this cluster, Rosencrans et al. (2024) simulated that external wakes cause about one-third of that loss.

Due to large-scale validation studies like Dörenkämper et al. (2020) and Williams (2025), the accuracy of WRF to estimate the wind resource without turbines is relatively well understood. However, modeling the momentum extraction, and consequently power generation, of turbines on a mesoscale grid that is typically an order of magnitude larger than the rotor area has proven to be difficult. The currently most established wind farm parameterization (WFP) was developed by Fitch et al. (2012), with an important bug-fix presented by Archer et al. (2020) rendering older results questionable. This Fitch parameterization was the first scheme that explicitly extracts momentum and adds turbulence to the flow. With the Fitch model typically showing an un-



derestimation of generated power for all wind directions, except for an overestimation when the turbines are aligned (Jiménez et al., 2015; Eriksson et al., 2015), several adaptation of this models have been presented. Redfern et al. (2019) aimed to include shear and veer over the rotor area, and building on that Wu et al. (2022) also added an air density correction. Abkar and Porté-
65 Agel (2015) and Mayol et al. (2020) suggested a data-driven correction for the turbine's induction zone, while Vollmer et al. (2024a) presented a physics-derived correction. As layout effects are not resolved, Pan and Archer (2018) proposed a method to correct for these effects. With similar reasoning, Ma et al. (2022a) coupled the Jensen engineering wake model to WRF. Lastly, the Explicit Wake Parameterization (EWP; Volker et al. (2015)) takes a different approach by including sub-grid-scale vertical wake expansion. As shown in Larsén and Fischereit (2021), this results in a wake deficit more spread out in the vertical
70 compared to Fitch. Additionally, the generation of turbine-induced turbulence is explicitly included in Fitch, but not in EWP, resulting in far lower turbulent kinetic energy (TKE) values when using the latter.

Pryor et al. (2022) showed that for the lease areas off the US East Coast and wind speeds below rated, EWP estimates a power production 25 % higher than Fitch. Ali et al. (2023) compared five parameterization with met mast, satellite and aircraft data of the cluster wake. Fitch and Redfern's WFP best matched the observed wind and turbulence levels, with EWP underestimat-
75 ing both TKE and the wake deficit. Abkar's WFP exhibited a high sensitivity to its tuning parameter, and Pan's layout-aware modification resulted in decreased power and a slightly larger wake deficit. Chang et al. (2026) demonstrated that for a high altitude wind farm, including density, rotor-equivalent wind speed and induction corrections increased the accuracy of power estimates compared to Fitch.

While comparisons between wind farm parameterizations exist, a comprehensive validation with the generated power of wind
80 farms and with that an assessment of the models' accuracy and a recommendation for their application, has not yet been carried out.

The objective of this study is to execute a large-scale validation of WRF's wind farm parameterizations with production data of multiple offshore wind farms over several years. This comprises of several components: (1) investigate the accuracy of energy yield estimates from seven wind farm parameterizations at different model resolutions, (2) assess the major sources of uncer-
85 tainty independently, (3) compare the sensitivity to atmospheric conditions and (4) provide recommendations for the future use of mesoscale models for wind resource assessment.

2 Methods

This section describes the mesoscale model configuration (Sect. 2.1), validation data overview and processing (Sect. 2.2) and a method to determine undisturbed turbines (Sect. 2.3).



Table 1. Relevant parameters of the WRF model setup.

Parameter	Setting
Planetary boundary layer scheme	MYNN level 2.5
Land use data	MODIS
Surface layer scheme	MYNN
Land surface model	Unified Noah
Microphysics scheme	WRF single-moment five-class
Longwave radiation scheme	RRTMG
Shortwave radiation scheme	RRTMG
Cumulus scheme	Kain-Fritsch (D01, D02 only)
Atmospheric boundary conditions	ERA5
Sea surface boundary conditions	OSTIA
Vertical resolution	61 eta levels
Nudging	Grid nudging above PBL
Domains	3 (4)
Resolution	18-6-2-(0.67) km
Nesting	one-way

90 2.1 WRF

2.1.1 Model configuration

This study utilized version 4.5.1 of the Weather Research and Forecasting (WRF, Skamarock et al. (2021)) model. The model setup was based on the one used in Cañadillas et al. (2022). This configuration was the product of many sensitivity tests carried out for the production of the New European Wind Atlas (Hahmann et al., 2020) and was further optimized and used for offshore wind applications in several studies (Gottschall et al., 2018; Gottschall and Dörenkämper, 2021; Cañadillas et al., 2022; zum Berge et al., 2024). The most relevant parameters can be found in Table 1. The simulation period was 4.5 years, from July 2017 to December 2021, and was split up in blocks of 10 days (+24 hours of spin up) to limit model drift. Figure 1a illustrates the one-way nested domains centered around the German Bight. One objective of this work is to assess the model sensitivity to the horizontal resolution. As such, simulations were carried out with either three nested domains, with the innermost domain having a resolution of 2 km, or an additional fourth nested domain with a resolution of 0.67 km. All wind turbines displayed in Fig. 1b were simulated from their commissioning date onward, hence simulations in earlier years contained fewer turbines. The colored turbines indicate the wind farms for which data was available in the study, while black turbines indicate the other simulated farms in the German and Danish waters of which no production data or information on operational state were available.

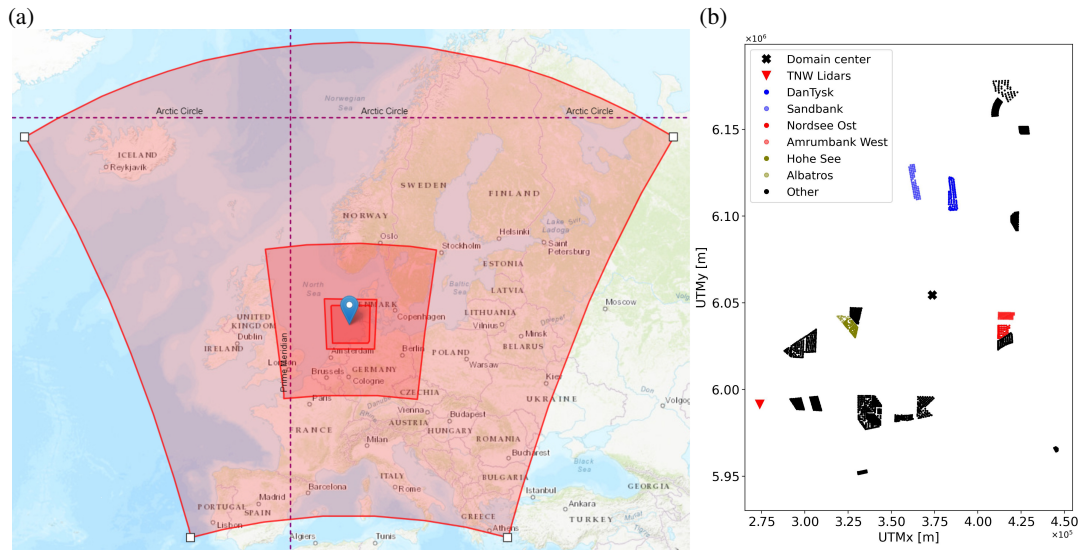


Figure 1. (a) Nested WRF domains centered around the German Bight, visualized using the WRF Domain Wizard tool (<https://jiririchter.github.io/WRFDomainWizard>). (b) Simulated wind farms, with the studied farms indicated in color. The domain center and the floating lidars at TNW are also indicated.

Table 2. Overview of Wind Farm Parameterizations, including reference papers and a short summary.

WFP	Abbreviation	Reference	Summary
Fitch	Fitch-O	Fitch et al. (2012)	Original: momentum sink and turbulence source
	Fitch-RE	Redfern et al. (2019)	Rotor equivalent instead of hub height wind speed
	Fitch-RE, ρ	Wu et al. (2022)	Model density instead of standard density
	Fitch-dAIM	Abkar and Porté-Agel (2015)	Data-driven axial induction modification
	Fitch-pAIM	Vollmer et al. (2024a)	Physics-driven axial induction modification
	Fitch-block	Pan and Archer (2018)	Include layout effects using geometric quantities
Explicit Wake Parametrisation	EWP	Volker et al. (2015)	Classic wake theory; no turbulence source

105 2.1.2 Wind farm parameterizations

Seven wind farm parameterizations have been evaluated in this work. The implementation of five WFPs from Ali et al. (2022, 2023) was used and two more WFPs (Fitch-RE, ρ and Fitch-pAIM) were added. All WFPs calculate the power and thrust coefficients by interpolating from prescribed look-up tables, which matched curves from installed turbines as closely as possible. Six of the WFPs are derived from the original Fitch parameterization, as can be seen from the overview in Table 2.

110 EWP was also included, providing an alternative that includes an initial vertical wake expansion. A more detailed description of each WFP can be found in the introduction and Appendix A.

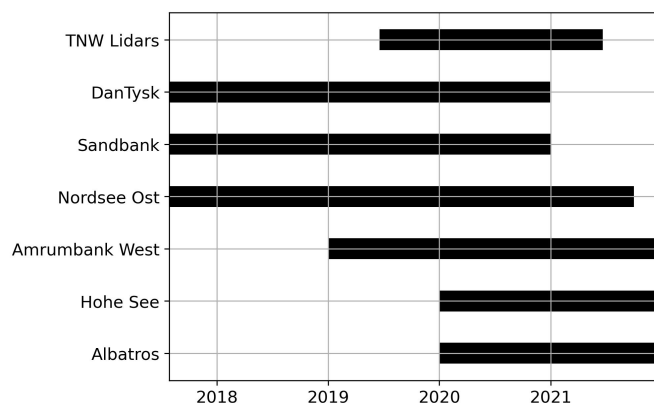


Figure 2. Data availability for the TNW floating lidars and the wind farms.

2.2 Validation data

2.2.1 Overview

SCADA data

115 The accuracy of the wind farm parameterizations was evaluated against SCADA (Supervisory Control And Data Acquisition) data from the wind farms' turbines. These data were provided by the wind farm operators in 10-min resolution on wind turbine level of six offshore wind farms in the German Bight, indicated in Fig. 1b. The length of the provided time period varied, as indicated in Fig. 2, but consisted of at least two years for each farm. Only the 10-minute averages of wind speed from the nacelle anemometer, the wind direction from the nacelle wind vane, and the generated power were used for analysis. Some
120 additional variables were used for filtering and gap-filling the data as explained in Section 2.2.2.

Two wind farms operated by Vattenfall in the north-east of the German EEZ consist of 80 Siemens 3.6 MW turbines with a hub height of 88 m and a rotor diameter of 120 m (DanTysk), and 72 Siemens 4 MW turbines with a hub height of 95 m and a rotor diameter of 130 m (Sandbank). RWE's wind farms further to the south close to the island Heligoland - in the so called trident cluster - consist of 80 Siemens 3.6 MW turbines with hub height at 90 m and a rotor diameter of 120 m (Amrumbank
125 West), and 48 Senvion 6.15 MW turbines with a hub height of 96.2 m and a diameter of 126 m (Nordsee Ost). The Hohe See and Albatros wind farms further to the west, operated by EnBW Hohe See GmbH & Co. KG, have Siemens 7 MW turbines with a hub height of 105 m and diameter of 154 m. Since the farms are adjacent, in this work, the 71 turbines from Hohe See and 16 turbines from Albatros were considered as one wind farm in this study.

130 Wind measurements

In addition to SCADA data, wind measurements from two profiling floating lidars at the TNW (Ten Noorden van de Waddeneilanden) site, indicated in Fig. 1b were used. This measurement campaign, conducted between June 2019 and June 2021,



was located west of the westernmost wind farm in the simulation domain. While this evaluation was based on a single point measurement within a domain of substantial spatial extent, hence where significant spatial variability is expected, the inclusion of these measurements was justified due to the large wind direction sector (including dominant wind directions) where the flow is undisturbed by wind farms. This enabled a meaningful, albeit limited, comparison between the model and observed data. The usage of other measurements closer to the studied wind farms in the period of interest was not possible as the offshore met masts FINO1 and FINO3 are both since several years surrounded by wind farms and the nacelle wind speed measurements from the SCADA data are too unreliable to be used as reference.

140 2.2.2 SCADA data processing

To ensure a fair comparison with the WRF results, the SCADA data was processed to derive a power time series in 10-min resolution that is representative for 100% turbine availability, hence eliminating non-normal operation like boosting, curtailment and downtime.

Variables used for this were power signal, the nacelle wind speed and wind direction and the pitch angle of one of the blades, all in 10-minute temporal resolution. The data was quality-controlled by flagging any missing and nonphysical values. The wind direction was used for the identification and filtering of inflow sectors. These measurements were corrected for two major errors sources: inconsistency and a wrong calibration to north. The inconsistency was assessed by comparing the weekly running wind direction averages of the individual turbines to that across all turbines. Discontinuities were detected using a threshold condition of a peak difference of at least 2° per day. The biases between the identified periods were removed to create a time-consistent wind direction signal. To correct the bias towards the north, a wake simulation was conducted, using the engineering wake modeling suite FOXES (Schmidt et al., 2023). For both simulation and measurements, the wind farm yield loss relative to undisturbed turbines was calculated. The bias of each wind direction measurement was minimized by matching the two wind-direction dependent wake loss distributions.

To flag curtailment and downtime, a polygon filter was used on the pairs of wind speed and power. Above rated wind speed, all power values below 98% of rated power were flagged. Below rated wind speed, a box filter was applied in the mean pitch to mean power domain to exclude pitch angles that deviated by more than 1° from the pitch angles of regular operation. To derive the power estimate at 100% turbine availability, a potential power was calculated for the flagged time stamps at each turbine, using the turbine power curves provided by the wind farm operators and a wind speed estimate at each turbine during downtime and curtailment. The wind speed estimate was calculated with a corrected 100 m reference wind speed from ERA5 (Hersbach et al., 2020). For the correction at every turbine a K-Nearest Neighbor (KNN) algorithm was used, trained during normal operation of the turbine, and using wind direction at the turbine and month of the year as features; the latter as a proxy for atmospheric stability.

The uncertainty of this potential power estimate was calculated using a Monte-Carlo approach by replacing the measured wind speed with the KNN-based wind speed estimate during random periods of normal operation and quantifying the difference between measured power and estimated power. The uncertainty of the energy yield estimate at 100% turbine availability is then the product of the length of the flagged periods and the uncertainty of the potential power estimate during these periods.



As an example, if the estimated power during downtime has an uncertainty of 10% and this turbine is not in normal operation 30% of the time, the overall estimated uncertainty at 100% turbine availability would be 3%. For the wind farms considered in this study, this overall uncertainty was estimated to range between 0.1% to 0.5%. For confidentiality reasons, the uncertainty is not displayed for each wind farm individually.

Lastly, it should be noted that operational information from surrounding wind farms is not available and therefore cannot be accounted for. In particular, upstream wind farms that generate external wakes may at times be curtailed or experience downtime, which would reduce their wake impact on the wind farms investigated in this study. As a result, the SCADA power is likely slightly underestimated, an effect that is particularly relevant for the analysis of external wakes in Sect. 3.5.2.

175 2.3 Identification of undisturbed turbines in model and measurement data

The analysis in Sect. 3.3 focuses on the reconstruction of the turbine's power curve from simulation results to verify whether the curves provided by the operators are used correctly by the different WFPs. To exclude the influence of wake effects, this analysis is restricted to undisturbed turbines. This section presents the method used to identify which turbines are undisturbed as function of wind direction.

180 Wake simulations were performed using FOXES, yielding estimates of generated power and ambient power, which is derived directly from the background flow assuming no wake losses. Four-dimensional wind speed, wind direction, turbulent kinetic energy converted to turbulence intensity assuming isotropic turbulence, as well as the air density at the surface from the 4.5 year long WRF simulation without turbines were passed to FOXES. All turbines in the domain were modeled in FOXES using the same specifications as in WRF.

185 Figure 3 illustrates the procedure for flagging a turbine as undisturbed using one turbine in the south-east of the Sandbank wind farm (marked red in Fig. 3b), which for certain wind directions is also waked by DanTysk. In Fig. 3a the ratio between the turbine's generated power and ambient power is shown (black line), together with a moving average (red line) over 45°. To flag a turbine as undisturbed in a certain wind direction, this ratio needs to exceed 0.99. In this example, the turbine is undisturbed in two narrow wind direction sectors, and affected by either internal wakes or DanTysk's wind farm wake in the other sectors.

190 To ensure that turbines in WRF are undisturbed, an additional step related to the gridded nature of the simulations is needed. An example is illustrated in Fig. 4, where 2x2 WRF cells each containing one turbine are drawn. For the purpose of this illustration, only the white turbine in cell (1,1) is extracting momentum from the flow, while the other red turbines are passive observers. For a wind direction perpendicular to the grid orientation (Fig. 4a), the momentum extracted from the grid cell (background color) is passed to cell (2,1) directly downstream. Note that the magnitude of the deficit and the wake recovery are arbitrary and just for illustration purposes. At a slightly different wind direction (Fig. 4b), part of the extracted momentum is transported to cell (1,2). While the engineering model FOXES will flag this turbine as undisturbed (FOXES wake shown as reference), in the mesoscale model WRF this turbine will produce less power. For this reason, a turbine can only be considered undisturbed when at least two neighboring cells do not contain any turbines. For this example 2x2 wind farm, turbine (1,1) has undisturbed inflow

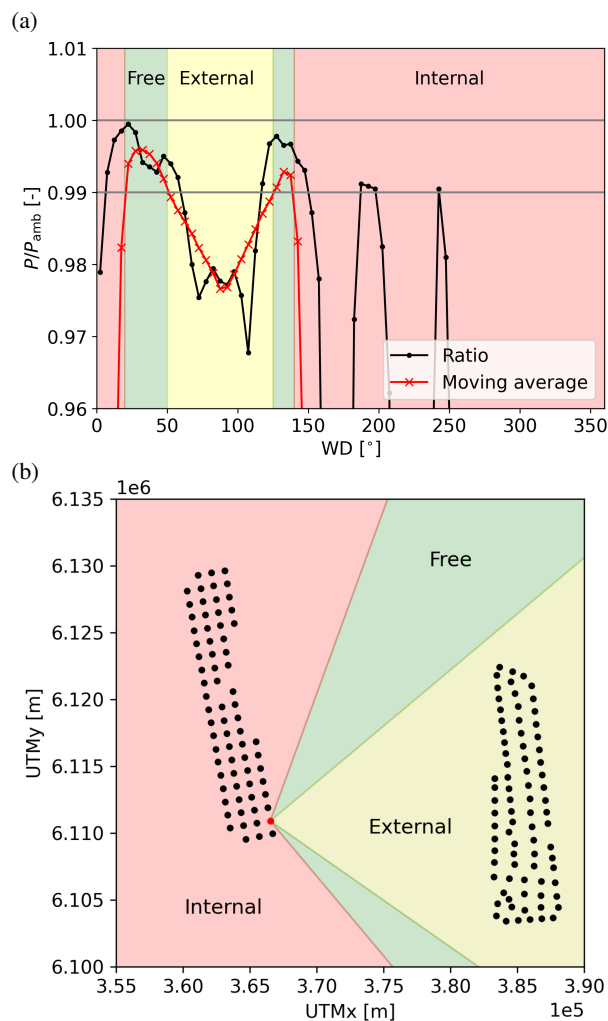


Figure 3. Illustrative example for identifying an undisturbed turbine using FOXES. (a) Ratio of generated power over ambient power (no wake losses) as function of wind direction. (b) Spatial representation of undisturbed (free) wind direction sectors of the considered turbine indicated in red.

200 for $180^\circ < WD < 270^\circ$ and turbine (1,2) for $270^\circ < WD < 360^\circ$. The turbine in Fig. 3 does not experience any free inflow in WRF.

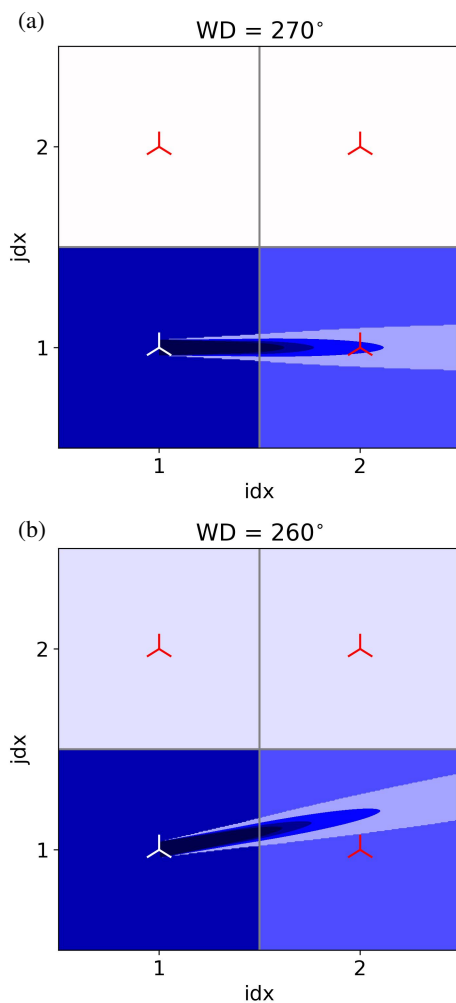


Figure 4. Sketch of transported momentum deficit (background color) for (a) $WD = 270^\circ$ and (b) $WD = 260^\circ$ of one wake producing turbine (white) and three reference turbines (red). For comparison, also the wake from FOXES is included.

3 Results

3.1 Total energy yield

The total energy yield is computed as the sum over all turbines for the entire period during which SCADA data was available. Figure 5 presents this total energy yield from the simulations normalized with the SCADA energy yield at 100 % availability (Sect. 2.2.2). Despite minor discrepancies in the details, the general trend is rather consistent between the wind farms. Fitch-O typically underestimates power by 3.1% to 4.5%. Modifications incorporating rotor-equivalent wind speed (RE) or the air density correction (ρ) yield minimal change. This reflects the offshore study area's relatively low wind shear and the - on

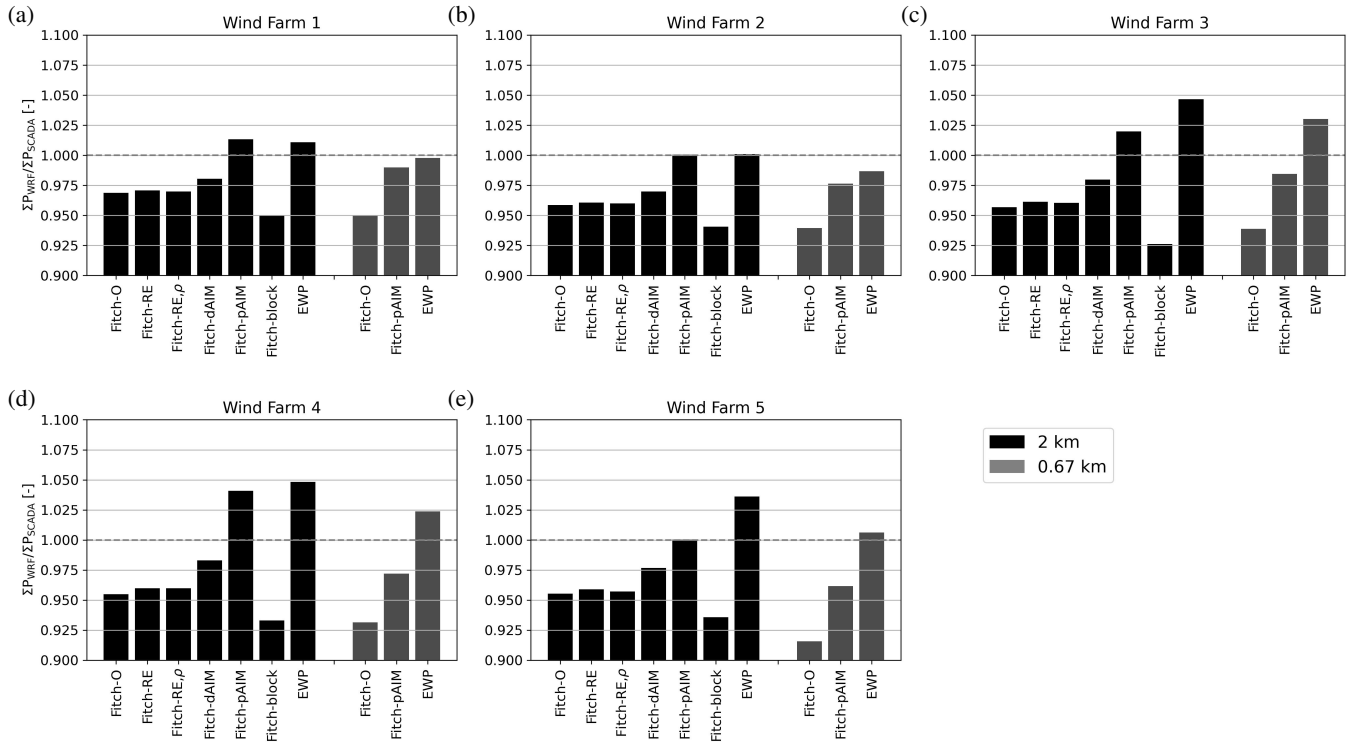


Figure 5. Total energy yield of the WFPs normalized by the energy yield at 100% availability calculated from SCADA for each wind farm. Black bars represent the results at low resolution (2 km) and grey bars the results at high resolution (0.67 km).

average - small difference of to the standard air density. WFPs incorporating axial induction modifications demonstrate the expected power increase. Fitch-dAIM continues to exhibit a power underestimation of several percent, whereas Fitch-pAIM generally overestimates power between 0.0% and 4.1%. Fitch-block shows a large underestimation of power, as it further decreases the power from Fitch-O by including internal wakes losses inside the grid cells. Other subgrid-scale WFPs like the Jensen WFP (Ma et al., 2022a) have the same issue and are therefore not included in this work. Lastly, EWP consistently overestimates power, with deviations of between 0.0% and 4.8%.

215 Based on this analysis, to make the detailed analysis presented in the remainder of the paper more concise, only results from Fitch-O, Fitch-pAIM and EWP are discussed as they represent the most fundamental differences between the WFPs.

To evaluate the sensitivity of the results to grid resolution, these three WFPs were run at a finer horizontal resolution of 0.67 km. The results of these simulations are presented on the right side of each panel of Fig. 5. All three models demonstrate an energy yield reduction compared to the coarser resolution, with Fitch-pAIM exhibiting the highest and EWP the lowest sensitivity to grid resolution.

220 While the total energy yield estimate remains the ultimate measure for a model's performance, it is a result of many factors, each contributing to the overall bias and uncertainty of the model. Therefore, the analysis in the following subsections attempts

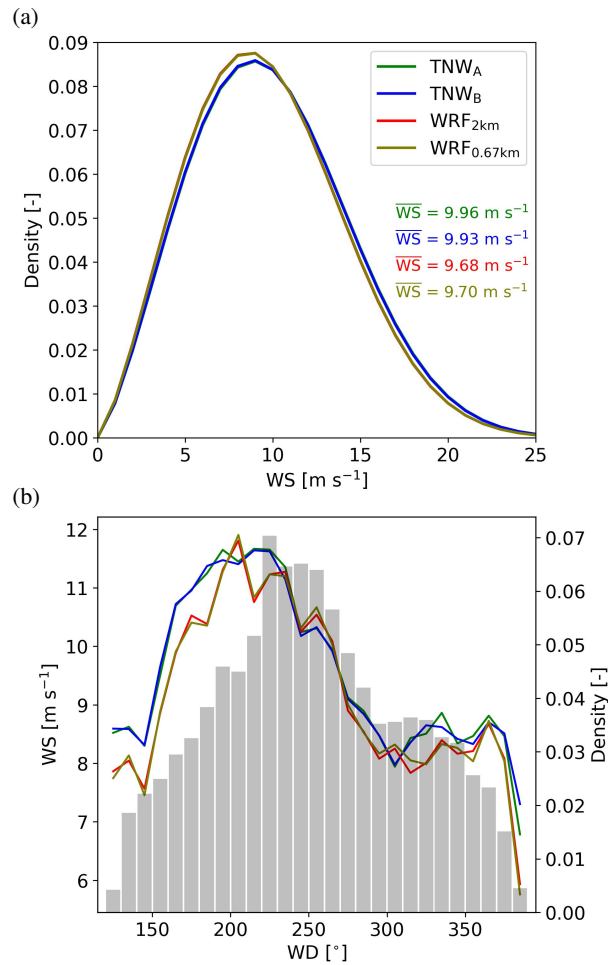


Figure 6. Comparison between measurements from two lidars (TNW_A and TNW_B) and WRF without turbines at two resolution. (a) Weibull distribution and annotated mean wind speed, (b) average wind speed per wind direction bin.

to look at the main factors individually. The uncertainty factors contributing to the energy yield estimate which are regarded to have the highest impact on the resulting model bias are the modelling of the wind speed (Sect. 3.2), the power curve (Sect. 225 3.3), internal losses (wakes and blockage; Sect. 3.4) and external wake losses (Sect. 3.5).

3.2 Wind speed uncertainty

Figure 6a illustrates the Weibull distribution for the two floating lidars at the TNW site (TNW_A and TNW_B) and the corresponding grid points in both WRF domains (WRF_{2km} and WRF_{0.67km}) for free inflow wind directions. The differences between the two lidars are negligible, as are those between the two WRF resolutions. The WRF distributions have a notable 230 leftward shift compared to the measurement, corresponding to an average bias of approximately -0.25 m s^{-1} . Figure 6b fur-

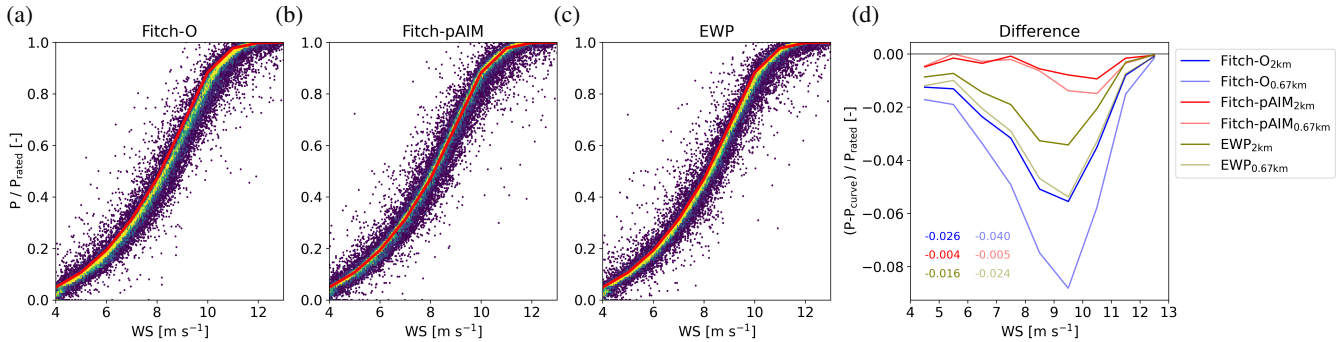


Figure 7. (a-c) Heatmaps of reconstructed power curve for one example wind farm for SCADA and three WFPs at 2 km resolution. The theoretical power curve is indicated with a red solid line. (d) Difference between reconstructed and theoretical power curve, normalized by the rated wind speed. Wind speed bins of 1 m s⁻¹ are used. Mean biases over all bins are indicated in the bottom left.

thermore demonstrates that this wind speed underestimation is consistent across wind directions, suggesting a systematic bias without clear directional dependencies. While this result cannot directly be transferred to the considered wind farms, it indicates that WRF most likely underestimates the wind speed at these sites. The observed underestimation falls well within the range of biases reported in the literature. For instance, Salvação and Guedes Soares (2018) examined locations off the Iberian coast and reported a mean annual wind speed bias over the open ocean ranging between -0.60 and -0.38 m s⁻¹ compared to satellite data. Closer to the shore, a comparison with buoy measurements indicated WRF biases of -0.07 to +0.59 m s⁻¹. Kalverla et al. (2019) analyzed four years of data from the IJmuiden met mast, located off the Dutch coast, and identified a bias of -0.25 m s⁻¹ at 27 m height and -0.5 m s⁻¹ at 115 m height. During the development of the New European Wind Atlas (NEWA), Hahmann et al. (2020) performed many sensitivity tests with different model configurations on several measurements sites. The model setup finally used to produce NEWA (Dörenkämper et al., 2020) was shown to have a mean wind speed bias of 0.21 ± 0.51 m s⁻¹ against validation data in simple terrain. Lastly, Cheynet et al. (2025) demonstrated that compared to offshore and coastal measurements at around 150 m height, NEWA showed a wind speed bias between -0.82 and +0.49 m s⁻¹. While the wind speed bias is relatively small, it has significant implications for subsequent power comparisons. To roughly estimate an energy yield bias from the wind speed distributions, the power curve of the generic NREL 5 MW turbine (Jonkman et al., 2009) was used. This exercise suggests an underestimation of the gross energy yield by WRF of around 3%, which means that a correction would effectively shift of the bars of simulated energy yield in Fig. 5 upwards.

3.3 Gross yield uncertainty

The second source of uncertainty concerns the gross yield, evaluating whether the actual reconstructed power curves of individual turbines accurately reflects the theoretical power curve provided by the wind farm operators. This assessment could not be made for SCADA data as no undisturbed wind speed measurements were available. This section instead addresses the question whether turbines modeled in WRF adhere to this prescribed curve correctly.



Undisturbed turbines of only one wind farm were considered, as the other farms had very few undisturbed turbines in WRF. Turbines were flagged as undisturbed using the methodology outlined in Sect. 2.3. For each time step, the average wind speed and power output of all turbines flagged as undisturbed were considered, hence one value per time step. Figure 7a-c show
255 heatmaps of this power curve reconstruction for one wind farm and the three WFPs, with the theoretical power curve displayed as a red solid line.

The results reveal a relatively high degree of scatter, arising from the decorrelation between the wind speed in a reference simulation without turbines (used here to determine the undisturbed wind speed) and the simulation with turbines (used for power). Among the WFPs, only Fitch-pAIM accurately reproduces the prescribed power curve. By contrast, Fitch-O and EWP
260 display a systematic underestimation, a finding consistent with the results of Vollmer et al. (2024a) and the motivation behind the development of Fitch-pAIM described in this publication.

Figure 7d depicts the deviation of each reconstructed power curve (the wind speed binned mean of Fig. 7a-c) from the theoretical one, with the mean over all bins annotated in the bottom left corner. Fitch-O and EWP exhibit a noticeable underproduction, while Fitch-pAIM lies closest to the theoretical curve with a small underproduction. Interestingly, the finer resolution results
265 in a significantly larger underestimation in Fitch-O and EWP. Just like the extracted momentum (wake effect), also the turbine induction is smeared out over the grid cell. The wind speed reduction due to induction, hence the difference between local grid cell wind speed and undisturbed wind speed, is therefore smaller for larger grid cells. When the local wind speed is used in power calculations, as done in Fitch-O and EWP, a turbine in a larger grid cell will produce more power. Fitch-pAIM does not have this limitation since it is using the induction-corrected free wind speed. Small deviation from the theoretical power curve
270 and differences between resolutions for Fitch-pAIM are attributed to an imperfect correction function f (see Appendix A), or are hypothesized to be due to the global blockage effect.

While the power curve reconstruction analysis does not allow for a quantification of a bias compared to the measurements, it reveals that both Fitch-O and EWP have a systematic error in the power curve calculations. This results in a systematic negative bias in the gross energy yield estimate of the modeled wind farms.

275 3.4 Uncertainty of internal wake and blockage losses

This section discusses the uncertainties associated with internal wake and blockage losses. The focus here lies on wakes, averaged over all conditions (Sect. 3.4.1), and for specific wind directions and boundary layer heights (Sect. 3.4.2). Patterns of global blockage are analyzed in Sect. 3.4.4.

3.4.1 Mean power per turbine

280 Figure 8 displays the Patterns of Production (PoPs), the mean generated power per turbine over the whole time series (three years) normalized by the maximum, for Amrumbank West. The SCADA PoP shows that turbines on the outer ring of the farm generate most power as they receive undisturbed inflow at times. Higher values on the west side of the farm are due to the dominant westerly wind. Turbines in the center experience losses of up to 13%.

At 2 km resolution, multiple turbines occupy one cell (up to nine, see Fig. B1b), indicated by identical colors. Compared to

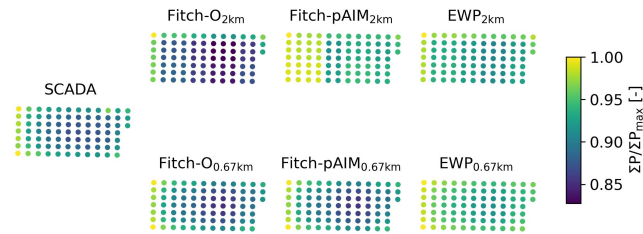


Figure 8. Amrumbank West Patterns of Production of total generated power per turbine, normalized by the maximum.

285 SCADA, Fitch-O displays systematically lower values, while EWP has higher values. At the finer resolution of 0.67 km, turbines do not share cells, and the patterns qualitatively match the SCADA PoP. Fitch-O again has a systematic underproduction, Fitch-pAIM shows a small underproduction but the gradient over the farms seems accurate, and EWP displays an overproduction with a very small gradient, indicating small wake losses.

To quantify these results, scatter plots based on these PoPs are displayed in Fig. 9 for all wind farms. The average power from
290 SCADA data is on the x-axis and the WFP estimate on the y-axis, meaning that values above the unity line indicate an overestimation of mean power by the model. The regression lines provide insight into the magnitude of the modeled wake deficit. Specifically, a regression line with a slope (indicated with annotated text) larger than unity indicates that the modeled wakes are stronger than those observed in the production data, whereas a slope smaller than unity suggests weaker modeled wakes.

At 2 km resolution, Fitch-O consistently underestimates power for all turbines across all farms (consistent with Fig. 5), and
295 tends to slightly overestimate the wake effect. In contrast, EWP demonstrates significantly weaker wakes resulting in a general overestimation of power. Fitch-pAIM shows the largest variability, having overly strong wakes in one farm, overly weak wakes in another one, and wakes of the appropriate magnitude in the remaining three farms.

At 0.67 km resolution, the power decreases across all WFPs. Consequently, the positive biases observed for Fitch-pAIM and EWP at 2 km diminish, while the negative biases for Fitch-O become more pronounced. The slopes of the regression lines
300 change significantly with no clear trend between farms or parameterizations. Noteworthy is that the slope of Fitch-pAIM's regression line is close to that of Fitch-O, indicating that the slightly increased thrust due to the induction-correction in Fitch-pAIM has only a small effect on the wake strength.

That EWP consistently shows an underestimation of the wake effect is likely due to the prescribed initial vertical expansion of the wake (see Appendix A), resulting in a higher hub height wind speed used for power calculations.

305 3.4.2 Specific wind conditions

While the mean PoP is helpful to evaluate the WFPs overall representation of internal wakes, responses to specific atmospheric conditions vanish due to averaging. To better understand the models' sensitivities, this section focuses on narrower wind direction sectors and wind speeds below rated ($6 \text{ m s}^{-1} < \text{WS} < 10 \text{ m s}^{-1}$).

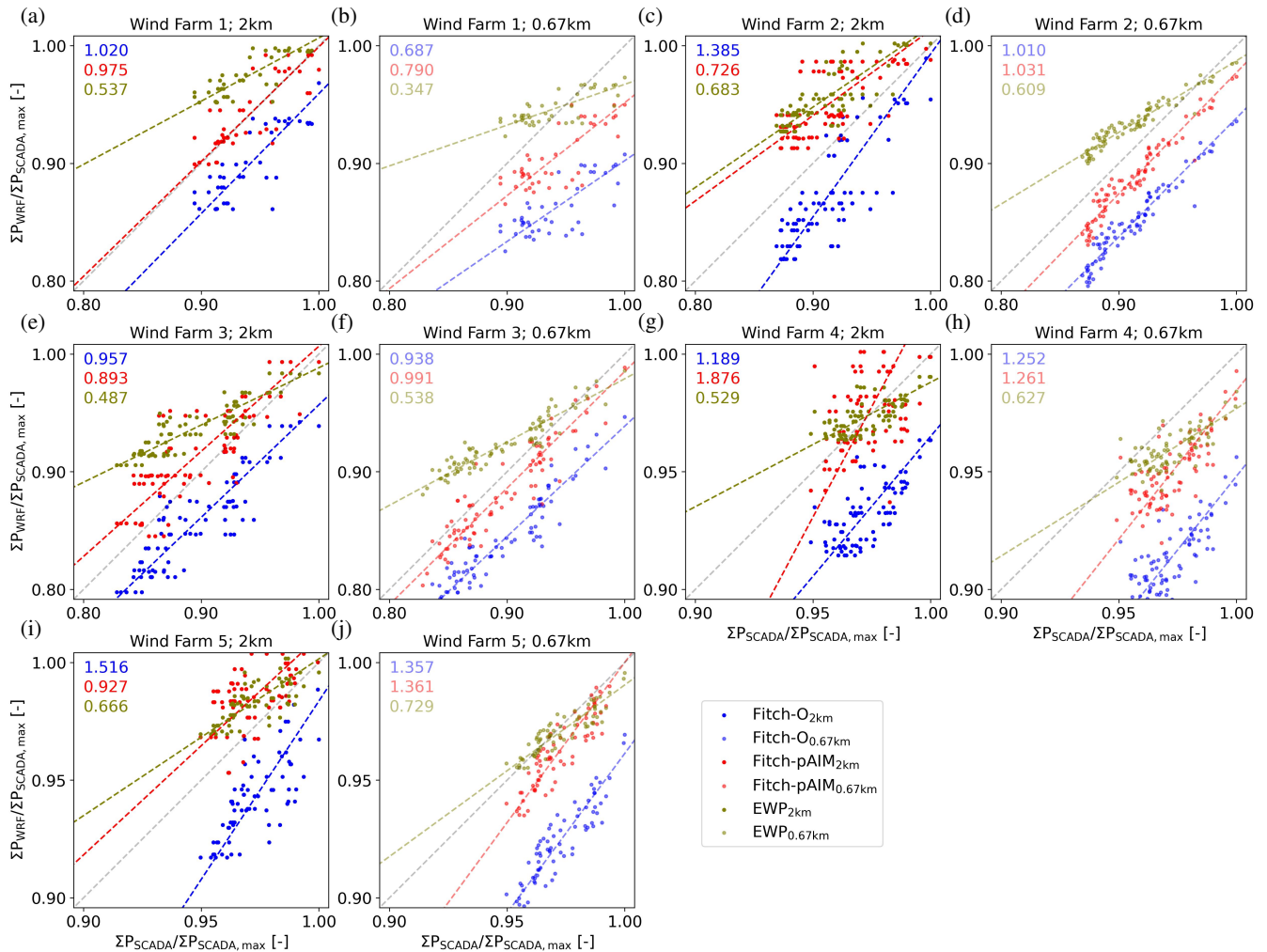


Figure 9. Scatter plots of total generated power per turbine, normalized by the maximum value in SCADA. Markers above the unity line indicate an overestimation of power by the model. Regression lines are fitted using Orthogonal Distance Regression (ODR), and their slopes are annotated in the figures. To preserve confidentiality, the order of wind farms is arbitrary and differs from that in Fig. 5.

Figure 10 shows PoPs for Amrumbank West, filtered for wind speeds below rated and one wind direction in which the turbines are aligned (Fig. 10a) and one in which they are staggered (Fig. 10b). In the aligned condition, SCADA illustrates a huge drop in power from the first to second row, which is not reproduced by any WFP at any resolution. The coarse resolution shows big step-wise power reductions between cells, whereas this is more gradual at finer resolution. In staggered conditions, the fine resolution simulations are able to accurately reproduce the pattern observed in SCADA apart from systematic biases, while at the coarse resolution the model results clearly show the effect of multiple turbines in a cell.

To highlight these findings further, Fig. 11 focuses on single rows of turbines in Amrumbank West (top) and Sandbank

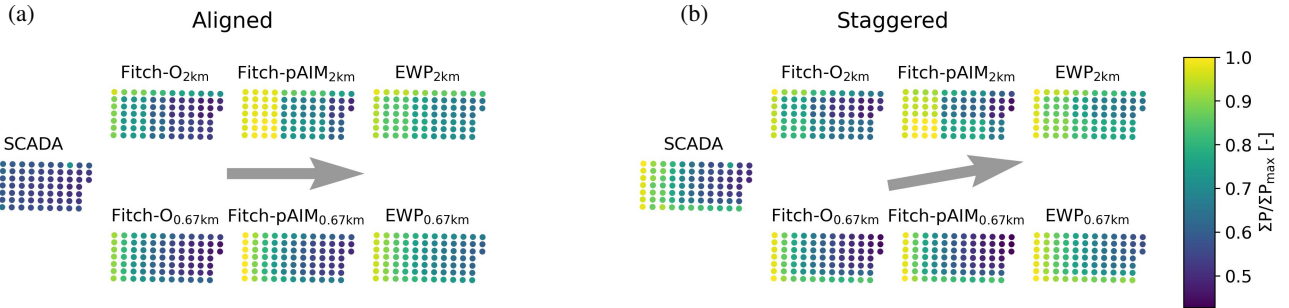


Figure 10. Patterns of production for Amrumbank West for $6 \text{ m s}^{-1} < WS < 10 \text{ m s}^{-1}$ for (a) aligned conditions $267.5^\circ < WD < 272.5^\circ$ and (b) staggered conditions $257.5^\circ < WD < 262.5^\circ$.

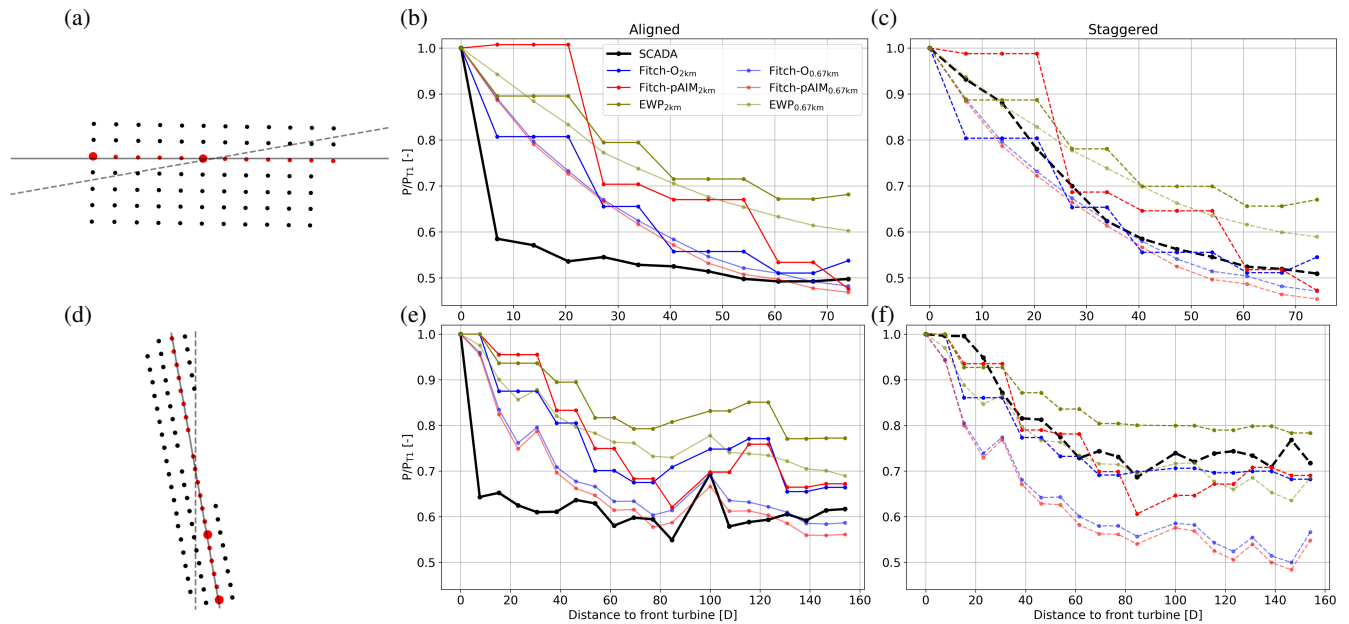


Figure 11. Single row analysis for Amrumbank West (a-c) and Sandbank (d-f) for $6 \text{ m s}^{-1} < WS < 10 \text{ m s}^{-1}$. Farm layouts are indicated in (a,d) with the studied turbines in red markers, the aligned wind direction ($267.5^\circ < WD < 272.5^\circ$ for Amrumbank West and $167.5^\circ < WD < 172.5^\circ$ for Sandbank) with a solid grey line and the staggered wind direction ($257.5^\circ < WD < 262.5^\circ$ for Amrumbank West and $177.5^\circ < WD < 182.5^\circ$ for Sandbank) with a dashed grey line. Power of each turbine, normalized by the front row turbine, are displayed in (b, e) aligned conditions and in (c, f) for staggered conditions.

(bottom). The farm layout, the selected turbine row, and the two wind directions under consideration (aligned and staggered) are illustrated in Fig. 11a,d. The other figures display each turbine’s power, normalized by the power of the front row turbine. For aligned cases (Fig. 11b,e), a substantial drop in power from the first to the second turbine is visible in SCADA. The WFPs



show a more gradual power reduction over the first few turbines. Clearly visible from their identical power is that several
320 grid cells contain multiple turbines in the 2 km simulation. The power output of downstream turbines tends to level out in
the measurements, which has been mentioned in the literature (e.g., Hancock, 2013; Bay et al., 2023). However, in the WRF
simulations, the power output continues to decrease along the row, which is particularly visible for the simulations at 0.67 km.
In the aligned cases (Fig. 11c,f), the measurements exhibit a more gradual reduction in power with downstream distance.
Especially visible at 0.67 km, there is a systematic difference between EWP and the others, with Fitch-O and Fitch-pAIM
325 being more accurate at Amrumbank West and EWP at Sandbank.

The thrust applied by the turbines is smeared over the whole grid cell as already shown in Fig. 4, explaining the model's inability
to represent the large drop in power at the second turbine. Modeled power values are actually almost the same in the aligned
and the staggered cases, as a wind direction difference of $\Delta WD = 10^\circ$ changes the wind speed deficit in a downstream grid
cell by $1 - \cos \Delta WD = 1.5\%$. For this reason, it cannot be expected from the mesoscale model to replicate the measurements
330 for such narrow wind direction sector. This indicates that aiming to reduce the difference between measurements and models
only for aligned conditions is not recommended.

A few other findings are noteworthy. The results for Fitch-pAIM at 2 km Fig. 11b show an unexpected pattern, as the power for
turbines 2-4 is higher than for the first turbine. This suggests that the assumption underlying Eq. A16, that the induction factors
of all turbines in a grid cell can be multiplied to correct the wind speed of the grid cell, does not hold universally. In Fig. 11e,f
335 at 2 km resolution, the second turbine has the same power as the front row turbine as they are placed in the same grid cell
(Fig. B1a), which consequently results in a very large deviation to the measurements in aligned conditions. This explains why
generated power decreases with increased resolution as already observed in Fig. 5. At 0.67 km, the second turbine experiences
a lower wind speed than at 2 km, leading to reduced power. This extends to all turbines that share a grid cell with others,
resulting in a significant reduction in generated power as the horizontal resolution of the simulation increases.

340 Next, a Side-by-Side comparison between two turbines, one undisturbed and one waked separated by several turbines, is pre-
sented. It should be noted that the power of the undisturbed turbine in the model used as a reference is not constant. It is
affected by a change in resolution, as the induction is also smeared out over the whole grid cell (Fig. 7). Additionally, the wind
speed deficit coming from neighboring cells affect the wind speed of the cell of the reference turbine (Fig. 4), the magnitude
of which is dependent on the wind direction. The results shown here should therefore be considered qualitatively only.

345 Figure 12a looks at two turbines in the same row in Amrumbank West as in Fig. 11a, indicated by the larger red markers. It
shows a steadily increasing power ratio (smaller wake losses) as the wind direction veers from 230° to 310° due to fewer
upstream turbines. This change is rather gradual in both measurements and WFPs, with the exception of $WD = 270^\circ$ where the
turbines are aligned. Here again the measurements show a significantly larger wake loss, which is not reproduced by any of
the simulations. Apart from consistent biases, both resolutions show the same pattern of result. EWP again models the weakest
350 wakes, but it is interesting to note that at 2 km Fitch-O has the lowest power ratio, whereas at 0.67 km this is Fitch-pAIM. The
higher thrust coefficient in Fitch-pAIM due to the axial induction corrected wind speed leads to stronger wakes, resulting in a
lower power ratio than Fitch-O at 0.67 km. At 2 km, however, this effect is outweighed by the issue of multiple turbines in one
cell, resulting in a higher power ratio than Fitch-O.

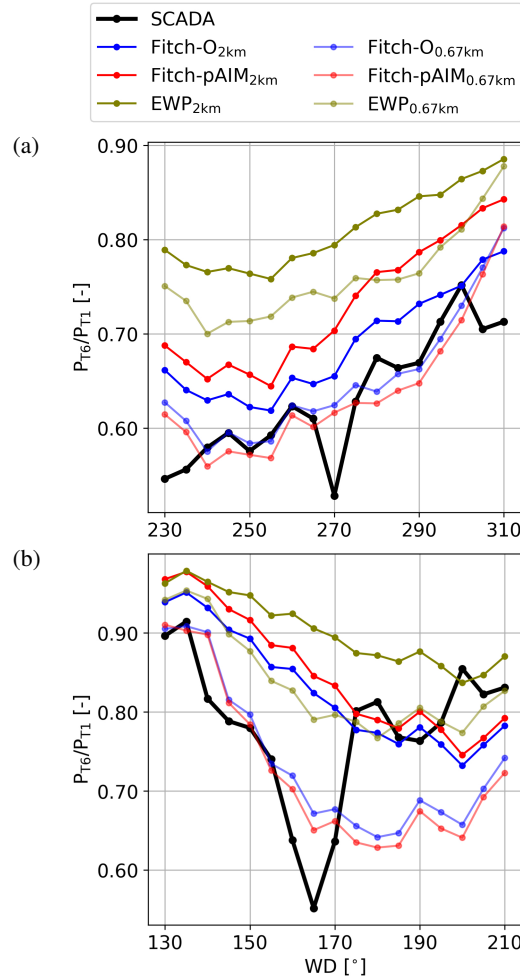


Figure 12. Power ratios between two turbines at Amrumbank West (a) and Sandbank (b) indicated by big red markers in Fig. 11a,d for a range of wind directions and $6 \text{ m s}^{-1} < WS < 10 \text{ m s}^{-1}$.

At Sandbank (Fig. 12b) the SCADA data displays a pattern symmetrical around the aligned condition at $WD = 170^\circ$, where wake losses are significantly larger than at other wind directions. This again is not reproduced by the WFPs, which show an asymmetry with larger losses for $WD > 170^\circ$. This is directly related to the larger number of turbines in the south-west corner of the farm compared to the south-east corner. The differences between WFPs and resolutions are similar to Fig. 12a.

The Side-by-Side analysis clearly further illustrates that mesoscale models are not able to capture the magnitude of wake effects when turbines are aligned, but might overestimate the wake effect when turbines are staggered.

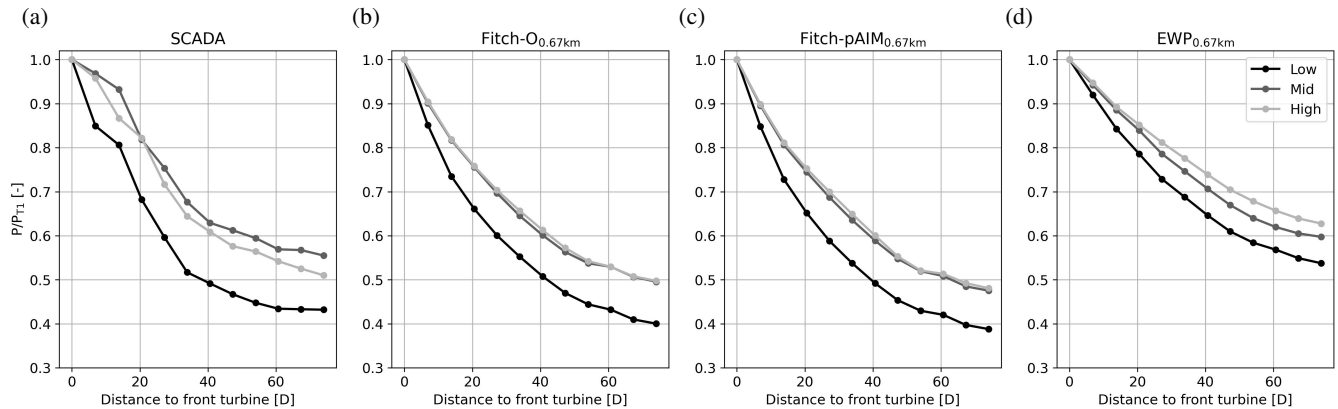


Figure 13. Effect of boundary layer height on the power deficit of a single row of turbines in Amrumbank West for a staggered wind direction. Classes are Low ($h_{BL} < 500$ m), Mid ($500 \text{ m} < h_{BL} < 1000$ m) and High ($h_{BL} > 1000$ m).

3.4.3 Sensitivity to the vertical structure of the atmosphere

This section investigates how the wake magnitude is affected by the vertical structure of the atmosphere. The planetary boundary layer height (h_{BL}) from the WRF model output was selected as filter metric, an alternative to any stability metric. Considered discrete classes were Low ($h_{BL} < 500$ m), Mid ($500 \text{ m} < h_{BL} < 1000$ m) and High ($h_{BL} > 1000$ m) boundary layers, which were determined from results of the WRF simulation without turbines. This WRF h_{BL} was also used to bin the SCADA data in the absence of a measurement, introducing some uncertainty. Focus of the analysis was to reproduce Fig. 11c, hence a single row analysis at staggered conditions in Amrumbank West under different h_{BL} . For brevity, only results from the finer resolution simulations are included.

The results in Fig. 13 illustrate that the difference between Mid and High boundary layers is small in the SCADA data, but that in Low boundary layers the power deficit is about 20% larger. This is physically sound, as low boundary layer heights are related to more stable conditions in which less mixing takes place and the vertical turbulent transport of momentum is reduced by the presence of the temperature inversion that caps the boundary layer. This dependency is rather well reproduced in WRF, where especially in Fitch-O and Fitch-pAIM the magnitude of the deficit is similar and no large difference between Mid and High boundary layers is observed. In EWP the deficits are consistently smaller, and there is a substantial difference between Mid and High boundary layers. It is hypothesized that this is due to the initial smearing of the extracted momentum, as explained in Appendix A.

These results indicate that WRF is well able to capture the physics associated with wake recovery under different atmospheric conditions.



3.4.4 Global Blockage

380 A direct quantification of global blockage is not possible by only using production data from a wind farm, as the pressure-driven
global blockage effect modifies the wind resource that is available to the wind farm compared to the hypothetical situation in
which there would be no wind farm. It also leads to a redistribution of momentum from front-row wind turbines to turbines
deeper inside the farm (Lanzilao and Meyers, 2022; Centurelli et al., 2024), an effect that can not be distilled from the data.
Rodaway et al. (2024) revealed the existence of global blockage by looking at the average power of the northern-most turbines
385 of Amrumbank West for slight deviations of the wind direction. This analysis was not possible with the mesoscale model, as
these turbines can only be considered as undisturbed for wind directions perpendicular to the grid orientation (as discussed
in Sect. 2.3). Instead, this section addresses the existence of blockage by showing the deceleration of wind speed from the
simulations upwind of the farm. The focus in Fig. 14 is on Amrumbank West due to its favorable orientation to study blockage
for westerly flow ($WD \approx 270^\circ$). The spatial plots, illustrating the wake deficit at 100 m of Fitch-pAIM relative to the simulation
390 without turbines, clearly depict the wake deficit, as well as the Kaskasi gap between the wind farms. However, the focus here
lies on the cells located immediately upstream of the first row of turbines. For both resolutions, it can be observed that the
first cell upstream has a lower wind speed than cells further upstream. Figure 14c illustrates the wind speed reduction as a
function of upstream distance along the cross-section indicated by the red solid lines, where $x = 0$ km denotes the center of the
cell containing the first turbine. At 2 km, the wind speed reduction one cell upstream slightly greater than two cells upstream.
395 At 0.67 km, a more gradual decrease in wind speed extending multiple upstream grid cells is visible, while the magnitude
is similar to that at 2 km. Approximately 10 km upstream of the wind farm, the wind speed deficit is still around 1%. This
reduction is not due to global blockage, but rather due to the external wakes originating from wind farms located 50 km to the
west (Hohe See, Albatros and Global Tech I, see Fig. 1b).

The physical accuracy of these observations requires further validation, which is considered beyond the scope of the current
400 work. However, it is noteworthy that the mesoscale model captures any wind speed reduction upstream of the wind farm, a
signature of global blockage. In the evaluation of the wind farm parameterizations, it can be considered another source of
uncertainty.

3.5 External wake loss uncertainty

This section evaluates how well external wakes (i.e., cluster wakes or wind farm wakes) are modeled by the WFPs. Section
405 3.5.1 studies the wind field between clusters, after which Sect. 3.5.2 investigates the effect on the power of front row turbines
of a downstream wind farm. As an illustrative example, the external wake effect on the Hohe See and Albatros wind farms is
shown, while similar phenomena are expected to occur at other wind farms in the studied domain. It should be noted that a
direct translation of these results into economic or contractual performance indicators of individual wind farms would not be
appropriate without further dedicated analysis.

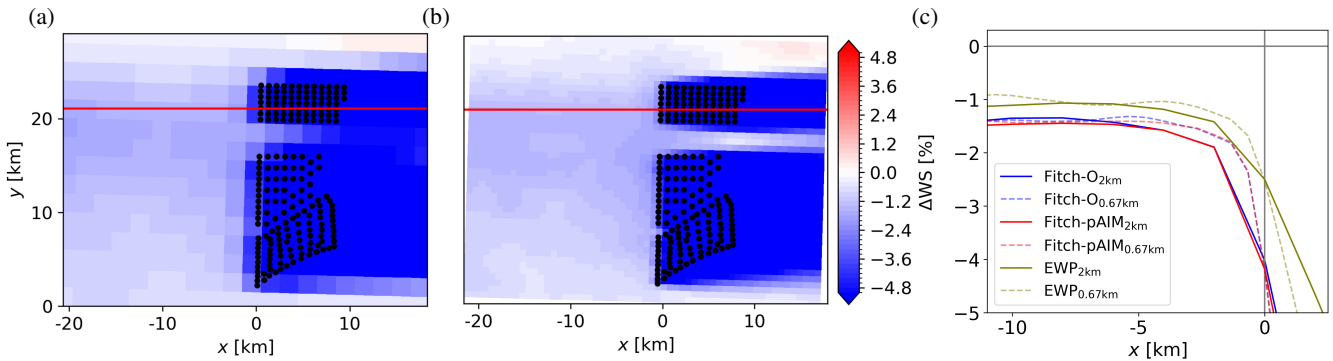


Figure 14. The effect of blockage on wind speed at Amrumbank West. Spatial plots of the wind deficit at 2 km (a) and 0.67 km (b) for Fitch-pAIM relative to the WRF simulation without turbines. (c) Wind speed deficits of all WFPs and resolutions as function of upstream distance along the red solid lines. All data filtered for $267.5^\circ < WD < 272.5^\circ$.

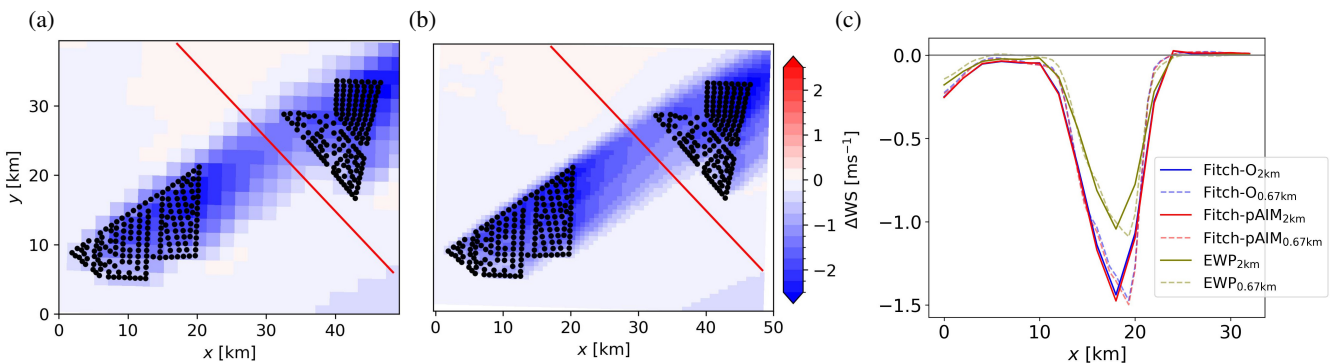


Figure 15. Wind speed deficit affecting Hohe See and Albatros at 2 km (a) and 0.67 km (b) resolution. (c) Wind speed deficits along the cross-section indicated by the red line in the spatial figures, taken from bottom-right to top-left.

410 3.5.1 Wind speed

This section analyzes the wind speed between upstream of Hohe See and Albatros. Validation of these results was not possible due to a lack of observational data, hence no lidar or flight data was available. Figure 15a-b illustrates the wind speed deficit modeled with Fitch-pAIM relative to a simulation without any turbines, at 100 m for a wind direction of 235° and all wind speeds. The difference in spatial resolution is clear from the granularity of these plots, but the magnitude of the wind speed deficit appears consistent across resolutions.

Figure 15c presents the wind speed deficit along the red solid line, reaching up to 1.5 m s^{-1} . Among the models, EWP exhibits again the weakest wake effects, while both Fitch-O and Fitch-pAIM display comparable deficits, with the latter showing a slightly more pronounced wind speed reduction due to increased thrust from the induction correction. The resolution does not appear to have a significant impact on the magnitude of the wake deficit. What can be seen is a slight shift of the location of

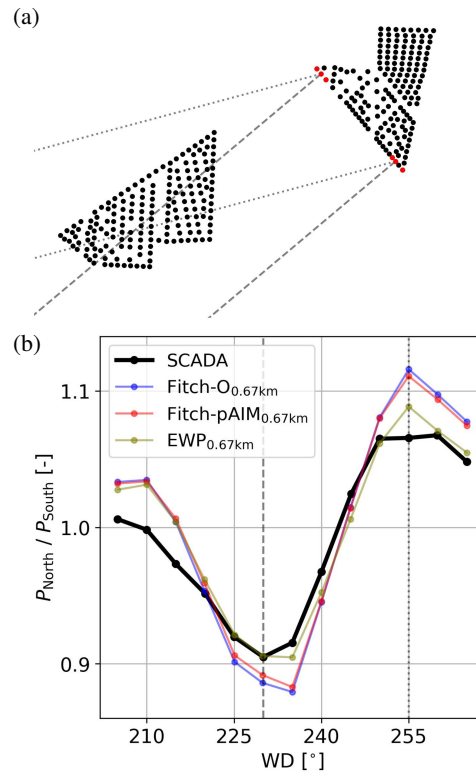


Figure 16. (a) Farm layout with the studied front row turbines as red markers. (b) Power ratio between the northern and southern turbines affected by a cluster wake for a range of wind directions. Two wind directions representing roughly the largest power losses are indicated by the dashed and dotted gray lines.

420 the maximum deficit and a larger gradient at the edge of the cluster wake, both due to the difference in grid resolution. As far as comparisons to existing literature allow, these results align well with previous findings. In a study focusing on several months of scanning lidar wind measurements in a wind farm cluster, Cañadillas et al. (2022) demonstrated a strong agreement between simulated cluster wakes from Fitch-O and lidar data, although a slight underestimation of the wake effect was observed. Similarly, in a comparison with FINO-1 data and airborne measurements, Ali et al. (2023) found that Fitch-O
425 generally captured the wind speed reductions under cluster wake conditions well, albeit also with a slight underestimation of the wake effect. Also in this work, EWP exhibited a much larger overestimation of wind speed.

3.5.2 Turbine power

This section focuses on the effect of the external wakes on the power ratio of front row turbines, averaged over three on the northern and three on the southern side, which has the same implication as discussed in Fig. 12. The turbines, indicated in
430 Fig. 16a, were carefully selected accounting for the effect discussed in Fig. 4, ensuring no influence from turbines in neighbor-



ing cells. For this reason, also only results for 0.67 km are shown. In contrast to Sect. 3.4, no wind speed filter was applied as deriving and undisturbed wind speed was not possible due to the external wake effect, so a wind speed bias between SCADA and model results cannot be excluded. By sweeping over wind direction sectors, conditions could be analyzed where either the northern three or southern three turbines is affected by the external wake.

435 The wake reaching the Hohe See and Albatros wind farms (Fig. 16b) causes a measurable but moderate reduction in power output at the selected front-row turbines. The magnitude of these effects is generally within the single-digit to low double-digit percentage range, depending on wind direction and with that the distance to the upstream wind farm. WRF does reproduce this asymmetry, with differences between the WFPs being small. EWP again produces the weakest wakes, which here provide the best agreement with the SCADA data, while Fitch-O and Fitch-pAIM tend to overestimate the wake losses. However, it should be noted that upstream wind farms are experiencing curtailment and downtime, which could not be accounted for in this analysis. As a result, the wake losses indicated by the SCADA data are likely slightly underestimated. Interestingly, Fitch-O has slightly higher wake losses than Fitch-pAIM, which is opposite to the wind speed deficit observed in Fig. 15c. This is due to the mean wind speed at the turbines, which is lower for the waked turbine and therefore likely in the steepest part of the power curve. A small axial induction correction of the wind speed in Fitch-pAIM therefore increases the power of the waked turbine more than the power of the undisturbed one, resulting in slightly smaller losses when looking at the power ratio. 445 While these findings should be interpreted qualitatively only, they strengthen the findings of Sanchez Gomez et al. (2024) that WRF is well able to capture the external wake effect, and with minimal differences between the parameterizations.

4 Discussion

This sections discusses the constraints under which this study was carried out, and therefore aspects that must be considered 450 when interpreting the presented results.

4.1 Wind speed bias

Different choices in the model setup (e.g., physics schemes, dynamics and global model forcing) lead to significant differences in the wind speed estimates, as shown in the sensitivity studies carried out in Hahmann et al. (2020). This study used a setup tailored to the area of interest and therefore had a relatively small mean wind speed bias of 0.25 m s^{-1} at the TNW lidar 455 location (Section 3.2), leading to a power difference of around 3% for a 5MW turbine. Note that this analysis excluded easterly wind and only evaluates a single point, while substantial variability could occur in the domain.

Where many studies get around this bias by evaluating wake losses instead, this requires a reliable estimate of the undisturbed wind speed, which in this study was not possible to obtain for the SCADA data due the many wake generating wind farms.

Considering the uncertainty related to wind speed, it is argued that the total power bias shown in Section 3.1 is not a valid 460 metric to assess which wind farm parameterizations is most accurate. While it is an attractive metric due to its simplicity, results are highly dependent on the wind speed distribution and the 'best' performing WFP can simply be due to errors cancelling out.



These results do allow for a comparison between WFPs, as the simulated background wind speed is the same.

The rest of the study attempted to assess the performance of the WFPs by taking wind speed difference out of consideration.

4.2 Wind farm parameterizations

465 Some consideration related to the modeled turbines should be mentioned. Firstly, in Fig. 5 is was shown that modification incorporating the rotor-equivalent wind speed and air density yielded minimal change, reflecting the offshore study area. It should be noted that at higher altitudes, these corrections are expected to have a larger impact as shown in Chang et al. (2026). Secondly, Mangara et al. (2019) illustrated that the number of vertical model levels inside the rotor area affects the amount of momentum extracted from the flow, where more levels resulted in more extracted momentum and therefore a larger wake
470 deficit. This also influences the results of this study, but is expected to affect all WFPs similarly. The sensitivity to the number of vertical levels should be considered in future work.

Thirdly, the distribution of turbines over cells affects the produced power, especially at courser resolution where turbines share cells. This is best illustrated by Fig. 11e,f, where at 2 km resolution the first two turbines share a cell and receive undisturbed wind. If these turbines were split between cells, the second turbine would generate less power. However, on the level of a full
475 wind farm over longer time this issue is expected to have a smaller effect than the spread between models.

Lastly, all wind farm parameterizations rely on at least one empirical (tuning) or correction factor, as can be seen from their equations in Appendix A. In this study, only default or recommended values were used, but calibrated values are expected to have a significant impact on the results.

Most Fitch-related WFPs use a correction factor for the TKE coefficient. It's default value of $\alpha_{\text{TKE}} = 0.25$ was proposed
480 by Archer et al. (2020), based on a small study comparing the turbine-generated TKE from Fitch with that of a single LES run containing one turbine in a neutral boundary layer at a wind speed of 9 m s^{-1} . While this factor barely affects the wind speed deficit in the cell in which the turbine is located, Ali et al. (2023) demonstrated it does influence the wake recovery and therefore the power of downstream turbines. A thorough assessment of this correction factor under a wide range of conditions is therefore highly recommended for future research.

485 Fitch-dAIM contains a correction factor that varies depending on wind farm configuration and needs to be tuned to a higher-fidelity data set varying wind speed and direction. While the accuracy of a fully calibrated Fitch-dAIM is expected to be high, generating a reference data set for the full German Bight is computationally not feasible.

Fitch-pAIM uses a correction factor to account for how much of the mesh cross-section is occupied by the turbine area. For simplicity, this correction assumes that the mesh orientation is aligned in north-south and west-east direction, which due to the
490 map projection is only true at the domain center. The figures in Appendix B, however, illustrate that the misalignment of the cells containing the wind farms of interest was quite small.

Fitch-block uses geometric quantities and a multiple linear regression function fitted to results from five LES runs of one wind farm at neutral stratification to define a correction function used in the tendency and power equations. Additionally it assumes that the maximum wake recovery distance is $20 D$, although especially wind farm wakes are known to last longer. While Fitch-
495 block was designed to reduce power compared to Fitch-O for aligned turbines, most of the time turbines are staggered and



simulated power is often underestimated. Since Fitch-block does not correct for this, Fitch-O can be considered its upper limit, which results in a large underestimation of power compared to production data. This is also the reason why other subgrid-scale parameterizations like Jensen (Ma et al., 2022a) were not included in this study, as these have the same limitations.

500 EWP relies on an initial length scale $\sigma_o = \frac{1}{2} \cdot \sigma_R \cdot D$ for the vertical wake expansion. Here, σ_R is a empirical parameter whose default value was tuned to measurements of a 2 MW turbine. It is however unknown how this value changes for other turbine types of different sizes and rated power, with the authors (Volker et al., 2015) noting that measurements of other turbines are needed to reassess its value.

4.3 Generalizability

505 Although this study considered data from six offshore wind farms situated in the German Bight, the geographical concentration raises the question of applicability to other regions. Provided that biases in wind speed distribution are similar, it is expected that the outcomes are transferable to other offshore sites globally. However, onshore environments are characterized by higher turbulence intensities and larger variability in atmospheric stability, which might not have been included in the current study. Furthermore, a more complex topography makes the vertical representation of the wake more relevant.

510 With continued advancements in turbine technology, future wind farms are expected to have turbines larger than 20 MW. The accuracy of existing wind farm parameterizations for the turbines of these scales is unknown. Nevertheless, it is expected that general findings of this work continue to hold. All WFPs except for Fitch-pAIM will systematically underestimate power at undisturbed turbines, EWP continues to generate substantially weaker wakes compared Fitch-O and Fitch-pAIM, while external wakes are well represented by all WFPs.

5 Conclusions

515 This study assessed the accuracy of seven existing wind farm parameterizations (WFPs) within the WRF model by a comparison with SCADA data from six offshore wind farms in the German Bight. Fitch modifications integrating air density and rotor equivalent wind speed showed a negligible influence on power production in the studied offshore region. The use of a subgrid-scale model to capture layout effects lead to substantial underestimation of power, while an uncalibrated, data-driven axial induction modification failed to demonstrate the expected improvements. A more detailed evaluation at spatial resolu-
520 tions of 2 km and 0.67 km was conducted for the three remaining parameterizations: the original Fitch scheme (Fitch-O), Fitch incorporating a physics-derived Axial Induction Modification (Fitch-pAIM), and the Explicit Wake Parameterization (EWP). Total energy yield estimates showed large variability between WFPs, but results were consistent between farms with Fitch-O underestimating and Fitch-pAIM and EWP overestimating power. With increasing resolution the estimated power decreased, attributable to a reduced number of turbines per grid cell and therefore enhanced internal wake effects. The main sources of
525 uncertainty were addressed in the remainder of the work.

An underestimation of 0.25 m s^{-1} of the mean wind speed, leading to an AEP difference of about 3%, was found compared to lidar data. While not generalizable to the locations of the considered wind farms due to variability in the simulation domain,



530 this result suggested a systematic underestimation of the energy yield by a few percent. Reconstruction of the power curve for undisturbed turbines revealed that only Fitch-pAIM approached the theoretical power curve, whereas both Fitch-O and EWP displayed a systematic underestimation of gross energy yield with a dependency on the grid resolution. Internal wakes were underestimated for aligned turbine configurations, whereas they tended to be overestimated in staggered conditions. Given that the spatial resolution of WRF restricts accurate representation of internal wakes in narrow wind direction sectors, power estimates should be evaluated only over broader wind direction sectors to ensure robustness. At finer resolution, both Fitch-O and Fitch-pAIM yielded accurate representations of average internal wake magnitudes. At the coarser resolution the variability
535 between wind farms was considerable, limiting the generalizability of the results. Consistent is that EWP underestimated the internal wake effect across all resolutions and sites. Lastly, the magnitude of external wakes was well captured by all WFPs across all resolutions.

The presented results should be interpreted with care due to the associated uncertainty, including deviations in mean wind speed, model configuration, and SCADA data uncertainty. Additionally, the applicability of the results for larger future turbines is unclear. Nevertheless, this study is believed to demonstrate that, at a resolution fine enough to allocate individual
540 turbines to separate grid cells, the Fitch-pAIM wind farm parameterization achieves the highest level of accuracy.

Code and data availability. The original WRF code can be downloaded from <https://github.com/wrf-model/WRF>. For the implementation of Fitch-O, Fitch-RE, Fitch-dAIM, Fitch-block and EWP, the code from Ali et al. (2022) was used. The code for Fitch-pAIM can be found in Sengers et al. (2024). The code for Fitch-RE, ρ was derived from the reference paper (Wu et al., 2022).
545 The TNW floating lidar data can be obtained from <https://offshorewind.rvo.nl/page/view/c26468f2-f44e-4d01-81c1-b0cc3de8787d/wind-en-water-tnw>. The wind turbine positions can be made available upon request. The site specific power and thrust curves and the wind farm production (SCADA) data originate from operating commercial wind farms and are therefore confidential and cannot be shared.



Appendix A: Wind farm parameterization equations

Fitch et al. (2012): Original Fitch Parameterization (Fitch-O)

550 The original Fitch parameterization calculates the turbine's thrust and induced turbulent kinetic energy (TKE) that affect the flow using the following equations:

$$\frac{\partial u_k}{\partial t} = -\frac{1}{2} \cdot C_T(U_h) \cdot u_k \cdot U_k \cdot A_{\text{rot},k} \quad (\text{A1})$$

$$\frac{\partial \text{TKE}_k}{\partial t} = \frac{1}{2} \alpha_{\text{TKE}} \cdot (C_T(U_h) - C_P(U_h)) \cdot U_k^3 \cdot A_{\text{rot},k} \quad (\text{A2})$$

in which subscript k indicates vertical level, subscript h hub height, U the horizontal wind speed and u its component along
 555 the x-axis. The momentum equation for the v component is analogous to Eq. A1, but omitted here for brevity. $A_{\text{rot},k}$ is the area occupied by the turbine rotor between two vertical model levels, resulting in a vertically varying momentum sink and turbulence source over turbine relevant heights. α_{TKE} is a correction factor that defaults to 0.25 as proposed by Archer et al. (2020). Power is finally calculated as:

$$P = \frac{1}{2} \cdot \rho_0 \cdot C_P(U_h) \cdot U_h^3 \cdot A \quad (\text{A3})$$

560 in which $\rho_0 = 1.23 \text{ kg m}^{-3}$ is the fixed standard air density and A the rotor area. When a grid cell contains more than one turbine, the individual turbine's contributions are simply summed up.

Redfern et al. (2019): Rotor equivalent wind speed (Fitch-RE)

Instead of using the hub height wind speed, this parameterization uses the rotor equivalent wind speed (U_{RE}) instead. It is
 565 determined over all model levels between lower tip and upper tip height:

$$U_{\text{RE}} = \sum_{k=1}^K \frac{A_{\text{rot},k}}{A} \cdot U_k \cdot \cos(\theta_k - \theta_h) \quad (\text{A4})$$

Here, $\cos(\theta_k - \theta_h)$ indicates the veer over the rotor area, as it is equal to the angle between the wind direction at the model level k and hub height, which is used to orient the turbine. The tendency and power equations are then:

$$\frac{\partial u_k}{\partial t} = -\frac{1}{2} \cdot C_T(U_{\text{RE}}) \cdot u_k \cdot U_k \cdot \cos(\theta_k - \theta_h) \cdot A_{\text{rot},k} \quad (\text{A5})$$

$$570 \frac{\partial \text{TKE}_k}{\partial t} = \frac{1}{2} \alpha_{\text{TKE}} \cdot (C_T(U_{\text{RE}}) - C_P(U_{\text{RE}})) \cdot U_k^3 \cdot \cos(\theta_k - \theta_h) \cdot A_{\text{rot},k} \quad (\text{A6})$$

$$P = \frac{1}{2} \cdot \rho_0 \cdot C_P(U_{\text{RE}}) \cdot U_{\text{RE}}^3 \cdot A \quad (\text{A7})$$

Wu et al. (2022): Density corrections (Fitch- ρ)

Instead of using the standard density $\rho_0 = 1.23 \text{ kg m}^{-3}$, here the model density at interpolated to hub height ρ_h is used. Besides a direct effect on the power equation, it also affects the used C_P and C_T . In the previous, these were determined by



575 interpolating given curves to the current wind speed. Now, the curves are shifted to account for density differences, which is done by correcting the wind speed used in the power and thrust coefficient curves:

$$U = U_0 \left(\frac{\rho_0}{\rho_h} \right)^{\beta(U_0)} \quad (\text{A8})$$

in which:

$$\beta(U_0) = \begin{cases} \frac{1}{3}, & \text{for } U_0 < 8 \text{ m s}^{-1} \\ \frac{1}{3} + \frac{1}{3} \frac{U_0 - 8}{5}, & \text{for } 8 \text{ m s}^{-1} < U_0 < 13 \text{ m s}^{-1} \\ \frac{2}{3}, & \text{for } U_0 \geq 13 \text{ m s}^{-1} \end{cases} \quad (\text{A9})$$

580 This effectively results in an adjusted set of curves for a non-standard air density. These corrected curves are then used in the interpolation to the current model wind speed to find C_T and C_P . The tendency and power equations can then be rewritten as:

$$\frac{\partial u_k}{\partial t} = -\frac{1}{2} \cdot C_T(U_h, \rho_h) \cdot u_k \cdot U_k \cdot A_{\text{rot},k} \quad (\text{A10})$$

$$\frac{\partial \text{TKE}_k}{\partial t} = \frac{1}{2} \alpha_{\text{TKE}} \cdot (C_T(U_h, \rho_h) - C_P(U_h, \rho_h)) \cdot U_k^3 \cdot A_{\text{rot},k} \quad (\text{A11})$$

$$P = \frac{1}{2} \cdot \rho_h \cdot C_P(U_h, \rho_h) \cdot U_h^3 \cdot A \quad (\text{A12})$$

585 Note that in this work the WFP Fitch-RE, ρ was used. This is simply a combination of Fitch-RE and Fitch- ρ , but was not presented here separately.

Abkar and Porté-Agel (2015): Data-driven Axial Induction Modification (Fitch-dAIM)

This parameterization addresses the issue that the horizontal wind speed in a grid cell can deviate significantly from the
 590 undisturbed wind speed assumed for the calculations in Eq. A1-A3. A correction factor $\zeta \equiv \frac{U_\infty}{U_h}$ is used, which varies in value depending on farm configuration and can be calibrated to results from a high-fidelity simulation. By using $\zeta = 1$, the momentum equations default back to Fitch-O, but the TKE tendency equation still differs because of an added axial induction factor a . Even though induction will also directly affect the power, the reference paper does not provide any changes to the power equations and therefore remains the same as Eq. A3.

$$595 \quad \frac{\partial u_k}{\partial t} = -\frac{1}{2} \cdot \zeta^2 \cdot C_T(U_h) \cdot u_k \cdot U_k \cdot A_{\text{rot},k} \quad (\text{A13})$$

$$\frac{\partial \text{TKE}_k}{\partial t} = \frac{1}{2} C_T(U_h) \cdot (1 - \zeta \cdot (1 - a)) \cdot \zeta^2 \cdot U_k^3 \cdot A_{\text{rot},k} \quad (\text{A14})$$

$$P = \frac{1}{2} \cdot \rho_0 \cdot C_P(U_h) \cdot U_h^3 \cdot A \quad (\text{A15})$$

600 Vollmer et al. (2024a): Physics-derived Axial Induction Modification (Fitch-pAIM)

This WFP aims to derive the free wind speed using the 1D momentum theory:

$$U_{\infty,h} = \frac{U_h}{(1-a)^n} \quad (\text{A16})$$



with n the number of turbines in the cell and a the axial induction factor calculated from the C_T with

$$a = 0.5(1 - \sqrt{1 - C_T(U_{\infty,h})}) \cdot f(\theta_h, \Delta x, A, D) \quad (\text{A17})$$

605 A correction function f is introduced to account for the how much of the mesh's cross-section is occupied by the turbine area A , considering the misalignment between mesh orientation and wind direction at hub height θ_h . Using the grid's wind direction θ_h at hub height:

$$f(\theta_h, \Delta x, A, D) = A \cdot (D \cdot \Delta x \cdot \min(|\frac{1}{\cos(\theta_h)}|, |\frac{1}{\sin(\theta_h)}|))^{-1} \quad (\text{A18})$$

with Δx the horizontal grid size and D the rotor diameter. The correction function f defaults to $A \cdot (D \cdot \Delta x)^{-1}$ when the turbine orientation is perpendicular to the mesh and $A \cdot (D \cdot \sqrt{2} \cdot \Delta x)^{-1}$ when it is diagonal to the mesh. Note that this correction function assumes that the mesh is perfectly aligned with north-south and west-east direction.

The corrected wind speeds U_{∞} and u_{∞} replace U and u in tendency and power equations:

$$\frac{\partial u_k}{\partial t} = -\frac{1}{2} \cdot C_T(U_{\infty,h}) \cdot u_{\infty,k} \cdot U_{\infty,k} \cdot A_{\text{rot},k} \quad (\text{A19})$$

$$\frac{\partial \text{TKE}_k}{\partial t} = \frac{1}{2} \alpha_{\text{TKE}} \cdot (C_T(U_{\infty,h}) - C_P(U_{\infty,h})) \cdot U_{\infty,k}^3 \cdot A_{\text{rot},k} \quad (\text{A20})$$

615
$$P = \frac{1}{2} \cdot \rho_0 \cdot C_P(U_{\infty,h}) \cdot U_{\infty,h}^3 \cdot A \quad (\text{A21})$$

Pan and Archer (2018): Blockage metrics for layout (Fitch_{block})

This WFP attempts to include wind farm layout effects, one often mentioned weakness of mesoscale WFPs. It should be noted that this is the GM model used in Ma et al. (2022b). It uses two geometric quantities derived from the wind direction and layout to estimate the magnitude of the wake effect, as proposed by Ghaisas et al. (2017):

- Blockage ratio (BR): fraction of rotor area blocked by rotor area of an upstream turbine.
- Inverse blockage distance (IBD): metric to define the distance to the upstream turbines

These quantities are then used in a multiple linear regression function fitted to an LES database to define a correction function $\psi = 0.9615 - 0.1549 \cdot \text{BR} - 0.0114 \cdot \text{IBD} \cdot L_{\infty}$, where $L_{\infty} = 20D$ is the maximum wake recovery distance. This indicates that ψ becomes smaller when the wake effect is larger. If the blockage ratio is non-zero, this correction function is then used to correct the local wind speed in the grid cell:

$$\frac{\partial u_k}{\partial t} = -\frac{1}{2} \cdot C_T(U_h \cdot \psi) \cdot \psi^2 \cdot u_k \cdot U_k \cdot A_{\text{rot},k} \quad (\text{A22})$$

$$\frac{\partial \text{TKE}_k}{\partial t} = \frac{1}{2} \cdot C_T(U_h \cdot \psi) \cdot \psi^2 \cdot U_k^3 \cdot a \cdot A_{\text{rot},k} \quad (\text{A23})$$

630
$$P = \frac{1}{2} \cdot \rho \cdot C_P(U_h \cdot \psi) \cdot \psi^3 \cdot U_h^3 \cdot A \quad (\text{A24})$$



with a again the axial induction factor.

Volker et al. (2015): Explicit Wake Parametrisation (EWP)

EWP explicitly models the wake expansion using classic wake theory by including a diffusion equation. Assuming a Gaussian
 635 wake shape, it vertically integrates between all WRF levels within the rotor area.

The equations can be written as follows:

$$\frac{\partial u_k}{\partial t} = -\frac{\sqrt{\pi/8}}{4} \cdot C_T(U_h) \cdot \frac{U_h^2}{\sigma_e \Delta x^2} \cdot \frac{u_k}{U_k} \cdot \xi \quad (\text{A25})$$

$$\sigma_e = \frac{U_h}{3 \cdot C_{\text{diff}} \cdot \Delta x} \left[\left(\frac{2 \cdot C_{\text{diff}} \cdot \Delta x}{U_h} + \sigma_o^2 \right)^{1.5} - \sigma_o^3 \right] \quad (\text{A26})$$

$$\sigma_o = \frac{1}{2} \cdot \sigma_R \cdot D \quad (\text{A27})$$

$$640 \quad \xi = e^{-\frac{(z-h)^2}{2 \cdot \sigma_e^2}} \quad (\text{A28})$$

$$\frac{\partial \text{TKE}_k}{\partial t} = 0 \quad (\text{A29})$$

$$P = \frac{1}{2} \cdot \rho_0 \cdot C_P(U_h) \cdot U_h^3 \cdot A \quad (\text{A30})$$

with Δx the horizontal grid resolution and C_{diff} the local (grid cell's) turbulent diffusivity coefficient. σ_e is the vertical wake
 extension resulting from turbulent diffusion of momentum, analogous to the dispersion of plumes. It contains an initial length
 645 scale σ_o , which relies on the tunable parameter σ_R , which has a default value of 1.7. Lastly, ξ determines how the extracted
 momentum is distributed vertically using a Gaussian function based on σ_e , with $z - h$ indicating the vertical distance of the
 model level to hub height. EWP assumes that turbine induced turbulence is small enough to be neglected, so no tendency
 equation for TKE is prescribed. Power is calculated according to Fitch-O (Eq. A3).

Appendix B: Simulation grids

650 This sections displays how the turbines are placed in the WRF grids. The black big grid indicates the 2 km simulation, while
 the grey small grid indicates the 0.67 km simulations. Cells that contain at least one turbine are shaded in light grey for the
 2 km and dark grey for the 0.67 km resolution. Note that all turbines that fall within one cell are effectively placed in the middle
 of the cell by WRF.

Lastly, is should be noted that turbines from Nordsee Ost and Meerwind wind farms (Fig. B1b) occasionally share a cell at 2
 655 km resolution, indicated by crosses. These turbines are removed from the analysis at both resolutions, as well as in the SCADA
 data.

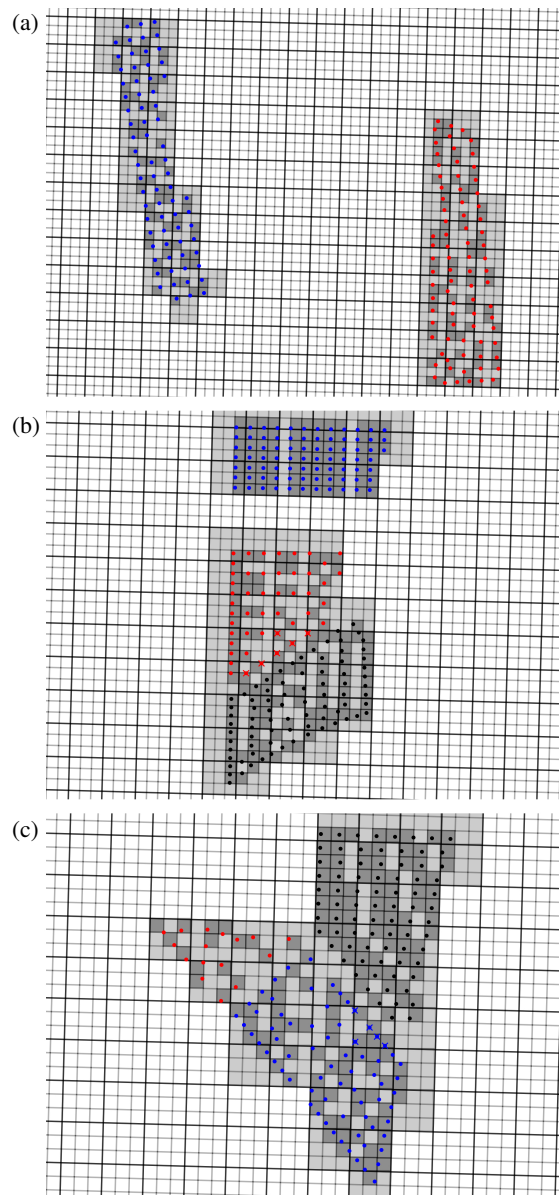


Figure B1. Layouts of wind farms on the WRF grid. (a) Sandbank (blue) and DanTysk (red). (b) Amrumbank West (blue) and Nordsee Ost (red), with Meerwind (black, not analyzed) to the south. (c) Hohe See (blue) and Albatros (red), with Global Tech One (black, not analyzed) to the Northeast. Crosses indicate turbines that share a cell with turbines from another farm and are not considered in the analysis.

Author contributions. BAMS prepared the WFP code, carried out the simulations, performed the analysis and wrote the manuscript. LV processed the SCADA data and wrote the related section, and was heavily involved in discussions. MD initiated the associated research



660 project and therefore was involved in the funding acquisition, and was involved discussions. LV and MD acquired the SCADA data. All authors reviewed the paper.

Competing interests. The authors declare that they have no conflict of interest.

Acknowledgements. The authors thank Vattenfall, RWE and EnBW Hohe See GmbH & Co. KG for providing the SCADA data, and specifically Sylvio Freitas (Vattenfall), Sam Williams (RWE) and David Wagner (EnBW AG) for valuable discussions.

665 The authors acknowledge the use of large language models (LLMs) to assist in refining and rewriting portions of this manuscript; however, the authors take full responsibility for the accuracy, integrity, and final content of this work.

670 This work was funded by the C2-Wakes (grant no. 03EE3087) project, funded by the German Federal Ministry for Economic Affairs and Energy (Bundesministerium für Wirtschaft und Energie) due to a decision of the German Bundestag, and funded by CETPartnership, the Clean Energy Transition Partnership under the 2023 joint call for research proposals, co funded by the European Commission (GA 101 069750) and with the funding organizations as detailed on <https://cetpartnership.eu/funding-agencies-and-call-modules>. The simulations were partly performed at the HPC cluster MOUSE (grant no. 03EE3067), located at the University of Oldenburg (Germany), funded by the German Federal Ministry for Economic Affairs and Energy (Bundesministerium für Wirtschaft und Energie) due to a decision of the German Bundestag. Additionally, the authors gratefully acknowledge the computing time made available to them on the high-performance computer Emmy at the NHR Center Göttingen. This center is jointly supported by the Federal Ministry of Education and Research and the state governments participating in the National High-Performance Computing (NHR) joint funding program (<http://www.nhr-verein.de/en/our-partners>).



675 References

- Abkar, M. and Porté-Agel, F.: A new wind-farm parameterization for large-scale atmospheric models, *J. Renew. Sustain. Ener.*, 7, 013–121, <https://doi.org/10.1063/1.4907600>, 2015.
- Ahsbahs, T., Nygaard, N. G., Newcombe, A., and Badger, M.: Wind Farm Wakes from SAR and Doppler Radar, *Remote Sens.*, 12, <https://doi.org/10.3390/rs12030462>, 2020.
- 680 Ali, K., Schultz, D. M., Revell, A., Stallard, T., and Ouro, P.: Assessment of five wind-farm parameterizations in the Weather Research and Forecasting model, <https://doi.org/10.48420/21262299>, [code] Last accessed: 27 June 2023, 2022.
- Ali, K., Schultz, D. M., Revell, A., Stallard, T., and Ouro, P.: Assessment of Five Wind-Farm Parameterizations in the Weather Research and Forecasting Model: A Case Study of Wind Farms in the North Sea, *Mon. Weather Rev.*, 151, 2333–2359, <https://doi.org/10.1175/MWR-D-23-0006.1>, 2023.
- 685 Archer, C. L., Wu, S., Ma, Y., and Jiménez, P. A.: Two Corrections for Turbulent Kinetic Energy Generated by Wind Farms in the WRF Model, *Mon. Weather Rev.*, 148, 4823–4835, <https://doi.org/10.1175/MWR-D-20-0097.1>, 2020.
- Baas, P., Verzijlbergh, R., van Dorp, P., and Jonker, H.: Investigating energy production and wake losses of multi-gigawatt offshore wind farms with atmospheric large-eddy simulation, *Wind Energ., Sci.*, 8, 787–805, <https://doi.org/10.5194/wes-8-787-2023>, 2023.
- Bastankhah, M. and Porté-Agel, F.: A new analytical model for wind-turbine wakes, *Renew. Energ.*, 70, 116–123, <https://doi.org/https://doi.org/10.1016/j.renene.2014.01.002>, special issue on aerodynamics of offshore wind energy systems and wakes, 2014.
- 690 Bastankhah, M. and Porté-Agel, F.: Experimental and theoretical study of wind turbine wakes in yawed conditions, *J. Fluid Mech.*, 806, 506–541, <https://doi.org/10.1017/jfm.2016.595>, 2016.
- Bay, C. J., Fleming, P., Doekemeijer, B., King, J., Churchfield, M., and Mudafort, R.: Addressing deep array effects and impacts to wake steering with the cumulative-curl wake model, *Wind Energ. Sci.*, 8, 401–419, <https://doi.org/10.5194/wes-8-401-2023>, 2023.
- C2Wind: Wake Modelling White Paper, White Paper 2-000-002-06-01, C2Wind, last accessed: 10 April 2025, 2025.
- Cañadillas, B., Beckenbauer, M., Trujillo, J. J., Dörenkämper, M., Foreman, R., Neumann, T., and Lampert, A.: Offshore wind farm cluster wakes as observed by long-range-scanning wind lidar measurements and mesoscale modeling, *Wind Energ. Sci.*, 7, 1241–1262, <https://doi.org/10.5194/wes-7-1241-2022>, 2022.
- 700 Cañadillas, B., Foreman, R., Barth, V., Siedersleben, S., Lampert, A., Platis, A., Djath, B., Schulz-Stellenfleth, J., Bange, J., Emeis, S., and Neumann, T.: Offshore wind farm wake recovery: Airborne measurements and its representation in engineering models, *Wind Energy*, 23, 1249–1265, <https://doi.org/https://doi.org/10.1002/we.2484>, 2020.
- Centurelli, G., Vollmer, L., Lukassen, L. J., and Peinke, J.: A new parametrization of the Global Blockage Effect, *J. Phys. Conf. Ser.*, 2767, 092110, <https://doi.org/10.1088/1742-6596/2767/9/092110>, 2024.
- 705 Chang, R., Sengers, B., Dörenkämper, M., and Gao, Z.: Modifications to a mesoscale wind farm parameterization enhance high-altitude wind farm simulations under real-world atmospheric conditions, *Renewable Energy*, 258, 125040, <https://doi.org/https://doi.org/10.1016/j.renene.2025.125040>, 2026.
- Cheyne, E., Diezel, J. M., Haakenstad, H., Breivik, Ø., Peña, A., and Reuder, J.: Tall wind profile validation of ERA5, NORA3, and NEWA datasets using lidar observations, *Wind Energ. Sci.*, 10, 733–754, <https://doi.org/10.5194/wes-10-733-2025>, 2025.
- 710 Christiansen, M. B. and Hasager, C. B.: Wake effects of large offshore wind farms identified from satellite SAR, *Remote Sens. Environ.*, 98, 251–268, <https://doi.org/https://doi.org/10.1016/j.rse.2005.07.009>, 2005.



- Dörenkämper, M., Olsen, B. T., Witha, B., Hahmann, A. N., Davis, N. N., Barcons, J., Ezber, Y., García-Bustamante, E., González-Rouco, J. F., Navarro, J., Sastre-Marugán, M., Sile, T., Trei, W., Žagar, M., Badger, J., Gottschall, J., Sanz Rodrigo, J., and Mann, J.: The Making of the New European Wind Atlas – Part 2: Production and evaluation, *Geosci. Model Dev.*, 13, 5079–5102, <https://doi.org/10.5194/gmd-13-5079-2020>, 2020.
- 715 Eriksson, O., Lindvall, J., Breton, S.-P., and Ivanell, S.: Wake downstream of the Lillgrund wind farm - A Comparison between LES using the actuator disc method and a Wind farm Parametrization in WRF, *J. Phys. Conf. Ser.*, 625, 012028, <https://doi.org/10.1088/1742-6596/625/1/012028>, 2015.
- EU: Ostend Declaration of Energy Ministers on the North Sea as Europe’s Green Power Plant, https://www.kefm.dk/Media/638179241345565422/Declaration%20ENERGY_FINAL_21042023.pdf, last accessed: 30 March 2025, 2023.
- 720 Fischereit, J., Schaldemose Hansen, K., Larsén, X. G., van der Laan, M. P., Réthoré, P.-E., and Murcia Leon, J. P.: Comparing and validating intra-farm and farm-to-farm wakes across different mesoscale and high-resolution wake models, *Wind Energ. Sci.*, 7, 1069–1091, <https://doi.org/10.5194/wes-7-1069-2022>, 2022.
- Fitch, A. C., Olson, J. B., Lundquist, J. K., Dudhia, J., Gupta, A. K., Michalakes, J., and Barstad, I.: Local and Mesoscale Impacts of Wind Farms as Parameterized in a Mesoscale NWP Model, *Mon. Weather Rev.*, 140, 3017 – 3038, <https://doi.org/10.1175/MWR-D-11-00352.1>, 2012.
- 725 Ghaisas, N. S., Archer, C. L., Xie, S., Wu, S., and Maguire, E.: Evaluation of layout and atmospheric stability effects in wind farms using large-eddy simulation, *Wind Energy*, 20, 1227–1240, <https://doi.org/https://doi.org/10.1002/we.2091>, 2017.
- Gottschall, J. and Dörenkämper, M.: Understanding and mitigating the impact of data gaps on offshore wind resource estimates, *Wind Energ. Sci.*, 6, 505–520, <https://doi.org/10.5194/wes-6-505-2021>, 2021.
- 730 Gottschall, J., Catalano, E., Dörenkämper, M., and Witha, B.: The NEWA Ferry Lidar Experiment: Measuring Mesoscale Winds in the Southern Baltic Sea, *Remote Sensing*, 10, <https://doi.org/10.3390/rs10101620>, 2018.
- Hahmann, A. N., Sile, T., Witha, B., Davis, N. N., Dörenkämper, M., Ezber, Y., García-Bustamante, E., González-Rouco, J. F., Navarro, J., Olsen, B. T., and Söderberg, S.: The making of the New European Wind Atlas – Part 1: Model sensitivity, *Geosci. Model Dev.*, 13, 5053–5078, <https://doi.org/10.5194/gmd-13-5053-2020>, 2020.
- 735 Hancock, P. E.: Wind Turbines in Series; A Parametric Analysis, *Wind Engineering*, 37, 37–58, <https://doi.org/10.1260/0309-524X.37.1.37>, 2013.
- Hasager, C. B., Vincent, P., Badger, J., Badger, M., Di Bella, A., Peña, A., Husson, R., and Volker, P. J. H.: Using Satellite SAR to Characterize the Wind Flow around Offshore Wind Farms, *Energies*, 8, 5413–5439, <https://doi.org/10.3390/en8065413>, 2015.
- 740 Hersbach, H., Bell, B., Berrisford, P., Hirahara, S., Horányi, A., Muñoz-Sabater, J., Nicolas, J., Peubey, C., Radu, R., Schepers, D., Simmons, A., Soci, C., Abdalla, S., Abellan, X., Balsamo, G., Bechtold, P., Biavati, G., Bidlot, J., Bonavita, M., De Chiara, G., Dahlgren, P., Dee, D., Diamantakis, M., Dragani, R., Flemming, J., Forbes, R., Fuentes, M., Geer, A., Haimberger, L., Healy, S., Hogan, R. J., Hólm, E., Janisková, M., Keeley, S., Laloyaux, P., Lopez, P., Lupu, C., Radnoti, G., de Rosnay, P., Rozum, I., Vamborg, F., Villaume, S., and Thépaut, J.-N.: The ERA5 global reanalysis, *Q. J. Roy. Meteor. Soc.*, 146, 1999–2049, <https://doi.org/https://doi.org/10.1002/qj.3803>, 2020.
- 745 Jensen, N. O.: A note on wind generator interaction, *Tech Rep Risø-M-2411*, Risø National Laboratory, https://orbit.dtu.dk/files/55857682/ris_m_2411.pdf, last access: 14 March 2024, 1983.
- Jiménez, P. A., Navarro, J., Palomares, A. M., and Dudhia, J.: Mesoscale modeling of offshore wind turbine wakes at the wind farm resolving scale: a composite-based analysis with the Weather Research and Forecasting model over Horns Rev, *Wind Energy*, 18, 559–566, <https://doi.org/https://doi.org/10.1002/we.1708>, 2015.



- 750 Jonkman, J. M., Butterfield, S., Musial, W., and Scott, G.: Definition of a 5-MW reference wind turbine for offshore system development: Technical Report, <https://doi.org/10.2172/947422>, 2009.
- Kalverla, P., Steeneveld, G.-J., Ronda, R., and Holtslag, A. A.: Evaluation of three mainstream numerical weather prediction models with observations from meteorological mast IJmuiden at the North Sea, *Wind Energy*, 22, 34–48, <https://doi.org/10.1002/we.2267>, 2019.
- Lanzilao, L. and Meyers, J.: Effects of self-induced gravity waves on finite wind-farm operations using a large-eddy simulation framework, *J. Phys. Conf. Ser.*, 2265, 022 043, <https://doi.org/10.1088/1742-6596/2265/2/022043>, 2022.
- 755 Larsén, X. G. and Fischereit, J.: A case study of wind farm effects using two wake parameterizations in the Weather Research and Forecasting (WRF) model (V3.7.1) in the presence of low-level jets, *Geosci. Model Dev.*, 14, 3141–3158, <https://doi.org/10.5194/gmd-14-3141-2021>, 2021.
- Lundquist, J. K., DuVivier, K. K., Kaffine, D., and Tomaszewski, J. M.: Costs and consequences of wind turbine wake effects arising from uncoordinated wind energy development, *Nature Energy*, 4, 26–34, <https://doi.org/10.1038/s41560-018-0281-2>, 2019.
- 760 Ma, Y., Archer, C. L., and Vasel-Be-Hagh, A.: The Jensen wind farm parameterization, *Wind Energ. Sci.*, 7, 2407–2431, <https://doi.org/10.5194/wes-7-2407-2022>, 2022a.
- Ma, Y., Archer, C. L., and Vasel-Be-Hagh, A.: Comparison of individual versus ensemble wind farm parameterizations inclusive of sub-grid wakes for the WRF model, *Wind Energy*, 25, 1573–1595, <https://doi.org/https://doi.org/10.1002/we.2758>, 2022b.
- 765 Mangara, R. J., Guo, Z., and Li, S.: Performance of the Wind Farm Parameterization Scheme Coupled with the Weather Research and Forecasting Model under Multiple Resolution Regimes for Simulating an Onshore Wind Farm, *Adv. Atmos. Sci.*, 36, 119–132, <https://doi.org/10.1007/s00376-018-8028-3>, 2019.
- Mayol, M. L., Diaz, G. N., Saulo, A., and Otero, A.: An induction-aware parameterization for wind farms in the WRF mesoscale model, *J. Phys. Conf. Ser.*, 1618, 062 006, <https://doi.org/10.1088/1742-6596/1618/6/062006>, 2020.
- 770 Mittelmeier, N., Allin, J., Blodau, T., Trabucchi, D., Steinfeld, G., Rott, A., and Kühn, M.: An analysis of offshore wind farm SCADA measurements to identify key parameters influencing the magnitude of wake effects, *Wind Energ. Sci.*, 2, 477–490, <https://doi.org/10.5194/wes-2-477-2017>, 2017.
- Montavon, C., Rodaway, C., Gunn, K., Smith, G., Dunsmore, D., Hoyo, M. D., and Sinclair, K.: Cluster Wakes and Their Effect on a Wind Farm Annual Energy Production: Are Current Models Capturing the Magnitude of the Effects Observed in Operational Data?, White paper, DNV, RWE, last access: 10 April 2025, 2024.
- 775 Nygaard, N. G.: Wakes in very large wind farms and the effect of neighbouring wind farms, *J. Phys. Conf. Ser.*, 524, 012 162, <https://doi.org/10.1088/1742-6596/524/1/012162>, 2014.
- Nygaard, N. G. and Hansen, S. D.: Wake effects between two neighbouring wind farms, *J. Phys. Conf. Ser.*, 753, 032 020, <https://doi.org/10.1088/1742-6596/753/3/032020>, 2016.
- 780 Nygaard, N. G. and Newcombe, A. C.: Wake behind an offshore wind farm observed with dual-Doppler radars, *J. Phys. Conf. Ser.*, 1037, 072 008, <https://doi.org/10.1088/1742-6596/1037/7/072008>, 2018.
- Nygaard, N. G., Steen, S. T., Poulsen, L., and Pedersen, J. G.: Modelling cluster wakes and wind farm blockage, *J. Phys. Conf. Ser.*, 1618, 062 072, <https://doi.org/10.1088/1742-6596/1618/6/062072>, 2020.
- Pan, Y. and Archer, C. L.: A Hybrid Wind-Farm Parametrization for Mesoscale and Climate Models, *Bound.-Lay. Meteorol.*, 168, 469–495, <https://doi.org/10.1007/s10546-018-0351-9>, 2018.
- 785 Pettas, V., Kretschmer, M., Clifton, A., and Cheng, P. W.: On the effects of inter-farm interactions at the offshore wind farm Alpha Ventus, *Wind Energ. Sci.*, 6, 1455–1472, <https://doi.org/10.5194/wes-6-1455-2021>, 2021.



- Platis, A., Siedersleben, S. K., Bange, J., Lampert, A., Bärfuss, K., Hankers, R., Cañadillas, B., Foreman, R., Schulz-Stellenfleth, J., Djath, B., Neumann, T., and Emeis, S.: First in situ evidence of wakes in the far field behind offshore wind farms, *Sci. Rep.*, 8, 2163, <https://doi.org/10.1038/s41598-018-20389-y>, 2018.
- Porchetta, S., Howland, M. F., Borgers, R., Buckingham, S., and Munters, W.: Annual wake impacts in and between wind farm clusters modelled by a mesoscale numerical weather prediction model and fast-running engineering models, *Wind Energ. Sci. Disc.*, 2024, 1–37, <https://doi.org/10.5194/wes-2024-58>, 2024.
- Pryor, S., Barthelmie, R., Shepherd, T., Hahmann, A., and Garcia Santiago, O.: Wakes in and between very large offshore arrays, *J. Phys. Conf. Ser.*, 2265, 022 037, <https://doi.org/10.1088/1742-6596/2265/2/022037>, 2022.
- Pryor, S. C., Barthelmie, R. J., and Shepherd, T. J.: Wind power production from very large offshore wind farms, *Joule*, 5, 2663–2686, <https://doi.org/10.1016/j.joule.2021.09.002>, 2021.
- Redfern, S., Olson, J. B., Lundquist, J. K., and Clack, C. T. M.: Incorporation of the Rotor-Equivalent Wind Speed into the Weather Research and Forecasting Model’s Wind Farm Parameterization, *Mon. Weather Rev.*, 147, 1029 – 1046, <https://doi.org/10.1175/MWR-D-18-0194.1>, 2019.
- Rodaway, C., Gunn, K., Williams, S., Sebastiani, A., Simon, E., Courtney, M., Thorsen, G. R., Clausen, E., Turrini, M., Wouters, D., Liu, Y., Gottschall, J., Dörenkämper, M., Patschke, E., Hung, L.-Y., and Adams, N.: OWA GloBE: Achieving Industry Consensus on the Global Blockage Effect in Offshore Wind, https://www.researchgate.net/publication/384562945_OWA_GloBE_Achieving_Industry_Consensus_on_the_Global_Blockage_Effect_in_Offshore_Wind, last accessed: 8th July 2025, 2024.
- Rohrig, K., Berkhout, V., Callies, D., Durstewitz, M., Faulstich, S., Hahn, B., Jung, M., Pauscher, L., Seibel, A., Shan, M., Siefert, M., Steffen, J., Collmann, M., Czichon, S., Dörenkämper, M., Gottschall, J., Lange, B., Ruhle, A., Sayer, F., Stoevesandt, B., and Wenske, J.: Powering the 21st century by wind energy—Options, facts, figures, *Applied Physics Reviews*, 6, 031 303, <https://doi.org/10.1063/1.5089877>, 2019.
- Rosencrans, D., Lundquist, J. K., Optis, M., Rybchuk, A., Bodini, N., and Rossol, M.: Seasonal variability of wake impacts on US mid-Atlantic offshore wind plant power production, *Wind Energ. Sci.*, 9, 555–583, <https://doi.org/10.5194/wes-9-555-2024>, 2024.
- Salvação, N. and Guedes Soares, C.: Wind resource assessment offshore the Atlantic Iberian coast with the WRF model, *Energy*, 145, 276–287, <https://doi.org/https://doi.org/10.1016/j.energy.2017.12.101>, 2018.
- Sanchez Gomez, M., Kelly, M., and Gottschall, J.: Can mesoscale models capture the effect from cluster wakes offshore?, *J. Phys. Conf. Ser.*, 2767, 062 013, <https://doi.org/10.1088/1742-6596/2767/6/062013>, 2024.
- Sanderson, C.: Wind theft: Five key issues Orsted, RWE and others are fighting over, <https://www.rechargenews.com/wind/wind-theft-five-key-issues-orsted-rwe-and-others-are-fighting-over/2-1-1784485>, recharge, March 10, 2025, 2025.
- Schmidt, J., Vollmer, L., Dörenkämper, M., and Stoevesandt, B.: FOXES: Farm Optimization and eXtended yield Evaluation Software, *J. Open Source Softw.*, 8, 5464, <https://doi.org/10.21105/joss.05464>, 2023.
- Schneemann, J., Rott, A., Dörenkämper, M., Steinfeld, G., and Kühn, M.: Cluster wakes impact on a far-distant offshore wind farm’s power, *Wind Energ. Sci.*, 5, 29–49, <https://doi.org/10.5194/wes-5-29-2020>, 2020.
- Sengers, B., Vollmer, L., and Dörenkämper, M.: First release of Axial Induction Factor correction of WRF Fitch in v4.2.1, <https://doi.org/10.5281/zenodo.12608856>, Zenodo [code]; Last accessed: 8th July 2025 , 2024.
- Siedersleben, S. K., Platis, A., Lundquist, J. K., Lampert, A., Bärfuss, K., Cañadillas, B., Djath, B., Schulz-Stellenfleth, J., Bange, J., Neumann, T., and Emeis, S.: Evaluation of a Wind Farm Parametrization for Mesoscale Atmospheric Flow Models with Aircraft Measurements, *Meteorol. Z.*, 27, 401–415, <https://doi.org/10.1127/metz/2018/0900>, 2018.



- 825 Skamarock, W. C., Klemp, J. B., Dudhia, J., Gill, D. O., Liu, Z., Berner, J., and Huang, X. y.: A Description of the Advanced Research WRF Model Version 4.3, Tech. Rep. NCAR/TN-556+STR, National Center for Atmospheric Research, <https://doi.org/10.5065/1dfh-6p97>, 2021.
- Souaiby, M. and Porté-Agel, F.: An improved analytical framework for flow prediction inside and downstream of wind farms, *Renew. Energ.*, 225, 120 251, <https://doi.org/https://doi.org/10.1016/j.renene.2024.120251>, 2024.
- Stieren, A. and Stevens, R. J.: Impact of wind farm wakes on flow structures in and around downstream wind farms, *Flow*, 2, E21, <https://doi.org/10.1017/flo.2022.15>, 2022.
- 830 Stieren, A. and Stevens, R. J. A. M.: Evaluating wind farm wakes in large eddy simulations and engineering models, *J. Phys. Conf. Ser.*, 1934, 012 018, <https://doi.org/10.1088/1742-6596/1934/1/012018>, 2021.
- Volker, P. J. H., Badger, J., Hahmann, A. N., and Ott, S.: The Explicit Wake Parametrisation V1.0: a wind farm parametrisation in the mesoscale model WRF, *Geosci. Model Dev.*, 8, 3715–3731, <https://doi.org/10.5194/gmd-8-3715-2015>, 2015.
- 835 Vollmer, L., Sengers, B. A. M., and Dörenkämper, M.: Brief communication: A simple axial induction modification to WRF’s Fitch wind farm parameterisation, *Wind Energ. Sci.*, 9, 1689–1693, <https://doi.org/10.5194/wes-9-1689-2024>, 2024a.
- Vollmer, L., Wurps, H., and Dörenkämper, M.: Benchmarking engineering wake models for farm-to-farm interactions, *Journal of Physics: Conference Series*, 2767, 092 095, <https://doi.org/10.1088/1742-6596/2767/9/092095>, 2024b.
- Williams, S.: Benchmarking numerically modelled data for wind resource assessment: a worldwide study, <https://www.linkedin.com/pulse/benchmarking-numerically-modelled-data-wind-resource-sam-williams-ihlmf/>, LinkedIn Pulse article; published April 16, 2025; Last accessed: 8th July 2025, 2025.
- 840 Wu, C., Luo, K., Wang, Q., and Fan, J.: A refined wind farm parameterization for the weather research and forecasting model, *Appl. Energ.*, 306, 118 082, <https://doi.org/10.1016/j.apenergy.2021.118082>, 2022.
- zum Berge, K., Centurelli, G., Dörenkämper, M., Bange, J., and Platis, A.: Evaluation of Engineering Models for Large-Scale Cluster Wakes With the Help of In Situ Airborne Measurements, *Wind Energy*, 27, 1040–1062, <https://doi.org/https://doi.org/10.1002/we.2942>, 2024.
- 845